JGR Oceans

RESEARCH ARTICLE
10.1029/2024JC021378

Parameterization of the Vertical Mixing for the Luzon Undercurrent in the Northern Western Pacific Ocean

Xianliang Chen[1], **Jianping Gan**[1], **Chiwing Hui**[1], **and James C. McWilliams**[2]

[1]Department of Ocean Science and Department of Mathematics, Center for Ocean Research in Hong Kong and Macau, The Hong Kong University of Science and Technology, Hong Kong, China, [2]Department of Atmospheric and Oceanic Sciences, University of California, Los Angeles, CA, USA

Key Points:

- Baroclinic pressure gradient force due to strong isopycnal tilting in the thermocline is crucial to the formation and maintenance of the Luzon Undercurrent (LUC)
- The strong isopycnal tilting is induced by locally enhanced vertical mixing. Nonlinearity and submesoscales also benefit the LUC formation
- A Munk-like adaptive mixing scheme is designed to capture the LUC, providing significant improvement over previous results

Correspondence to:

J. Gan,
magan@ust.hk

Citation:

Chen, X., Gan, J., Hui, C., & McWilliams, J. C. (2024). Parameterization of the vertical mixing for the Luzon Undercurrent in the northern western Pacific Ocean. *Journal of Geophysical Research: Oceans*, *129*, e2024JC021378. https://doi.org/10.1029/2024JC021378

Received 29 MAY 2024
Accepted 15 OCT 2024

Author Contributions:

Conceptualization: Xianliang Chen, Jianping Gan
Data curation: Xianliang Chen, Chiwing Hui
Formal analysis: Xianliang Chen, Jianping Gan, Chiwing Hui
Funding acquisition: Jianping Gan
Investigation: Xianliang Chen, Jianping Gan, James C. McWilliams
Methodology: Xianliang Chen, Jianping Gan, James C. McWilliams
Project administration: Jianping Gan
Resources: Jianping Gan
Software: Jianping Gan, Chiwing Hui
Supervision: Jianping Gan
Validation: Xianliang Chen, Jianping Gan, Chiwing Hui, James C. McWilliams
Visualization: Chiwing Hui
Writing – original draft: Xianliang Chen

Abstract The Luzon Undercurrent (LUC) is one of the most significant western boundary undercurrents in the northern western Pacific Ocean (WPO), essential for subsurface water transport and connecting subtropical–equatorial circulations. Over the last three decades, abundant observational progress has been made in revealing the basic features of the LUC. However, the dynamics and thus successful modeling of the LUC remain unresolved. In this work, we conducted a high-resolution (3 km, 60 levels) numerical investigation of the WPO circulation using the China sea multi-scale ocean modeling system. We paid particular attention to the vertical mixing, aiming to reasonably resolve the LUC by modifying the vertical mixing parameterization. Based on physics reasoning and experiments of physically based modeling, we designed an adaptive mixing scheme (AMS), which used a Munk-like function in the thermocline for enhanced vertical mixing in the areas of small Richardson numbers. Using the AMS, we reproduced the two-layer WPO circulations well and captured the inshore component of the LUC consistent with observations. Furthermore, we studied the dynamics of the LUC by analyzing the momentum balance and found that the LUC is primarily maintained by baroclinic pressure gradient force due to strong thermocline tilting near the western boundary. Enhanced vertical mixing in this highly sheared region crucially provides sufficient geostrophic support to sustain the LUC. Also, nonlinearity and submesoscale motions contribute positively to the LUC. This work advances physical understanding of the current-undercurrent system and improves numerical capability in capturing the LUC and WPO circulations.

Plain Language Summary In the northern western Pacific Ocean (WPO), there exists complex undercurrents below the upper layer (depth ~500–1,500 m), which flow in the opposite direction from the strong circulation in the upper ocean (depth <~500 m). The undercurrents are significant for subsurface transport and connecting subtropical-equatorial circulations; together with the upper circulation, they form the WPO circulation system. The undercurrents are less understood and their underlying physics remains unclear. In this study, we investigate the Luzon Undercurrent (LUC), which flows southward beneath the northward Kuroshio to the east coast off Luzon Island. Abundant observational works have unveiled the characteristics of the LUC, but little attention was paid to its dynamics. So far, the LUC is poorly resolved in prevailing global/regional ocean models. In this work, we developed an adaptive mixing scheme based on physics reasoning and modeling experiments, such that the LUC physics can be resolved and well reproduced in our regional model. Furthermore, we revealed the dynamics of the LUC and summarized key factors to its formation and maintenance. This work advances our physical understanding toward the undercurrents and improves numerical capability in simulating the LUC and WPO circulations.

1. Introduction

In the northern western Pacific Ocean (WPO), there are complex upper-layer current and middle-layer undercurrent circulations as illustrated in Figure 1. In the upper layer, the westward North Equatorial Current (NEC) bifurcates into the northward Kuroshio Current (KC) and the southward Mindanao Current (MC), forming the NEC–KC–MC (NKM) circulation system near the east coast of the Philippine Islands (Hu et al., 2020; Kashino et al., 2009; Nitani, 1972; Qiu & Lukas, 1996). In the middle layer, there is an undercurrent system NKMU, comprised of the North Equatorial Undercurrent (NEUC), the Luzon Undercurrent (LUC), and the Mindanao Undercurrent (MUC) (Hu et al., 2013; Li & Gan, 2020, 2022a; Qu et al., 1997; Schönau & Rudnick, 2017). The KC and MC are strong western boundary currents (WBCs), playing an essential role in the transport of freshwater, heat and energy, and in the dynamic interaction between WPO and neighboring marginal seas, such as the South China Sea (SCS) (Chern et al., 1990; Gan, Liu, & Hui, 2016; Guo et al., 2006; Nan et al., 2015). The MUC and

Writing – review & editing:
Jianping Gan, James C. McWilliams

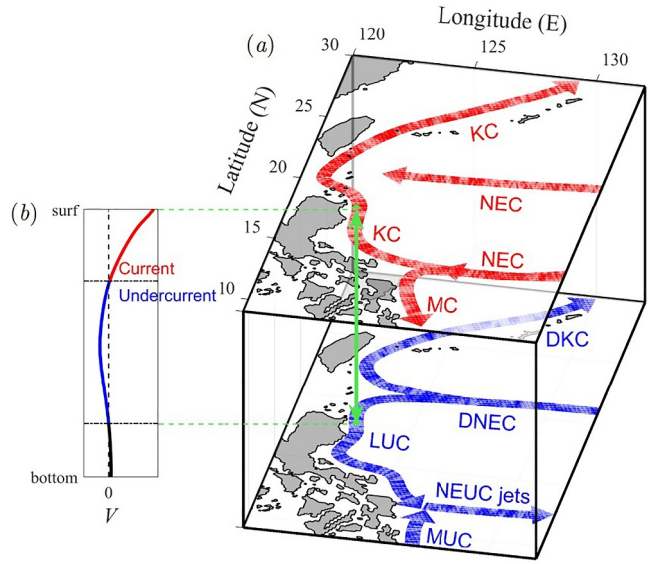

Figure 1. (a) Schematic showing the main currents in the two-layer WPO circulations. The upper-layer currents (red arrows) are the North Equatorial Current, Kuroshio, and Mindanao Current. The middle-layer currents (blue arrows) are the Luzon Undercurrent, Mindanao Undercurrent, and the North Equatorial Undercurrent jets. Panel (b) illustrates the meridional velocity profile of the KC–LUC system (Hu et al., 2020; Li & Gan, 2020, 2022a; Qu et al., 1997; Wang et al., 2014).

LUC are western boundary undercurrents (WBUCs), significant in conveying subsurface water masses and connecting subtropical and equatorial circulations (Hu et al., 2020; Qu et al., 1997; Wang et al., 2014).

The existence of the LUC was reported by Hu and Cui (1989) through analyzing the hydrographic data from cruises. Subsequently, Qu et al. (1997) demonstrated the basic structure of the LUC using conductivity temperature depth (CTD) data. The LUC is located right beneath the KC with only ∼50 km wide, and its maximum geostrophic velocity is evaluated to be ∼7 cm/s. Meanwhile, the LUC contains inshore and offshore cores. The inshore core, attached to Luzon Island (LI), extends downward from the KC bottom at ∼500 m, and the offshore core is the continuation of the surface offshore of the KC. These observations were supported by different data sets as gathered in Figure 2a for reference. Another key feature of the LUC is its intra-seasonal variation at a

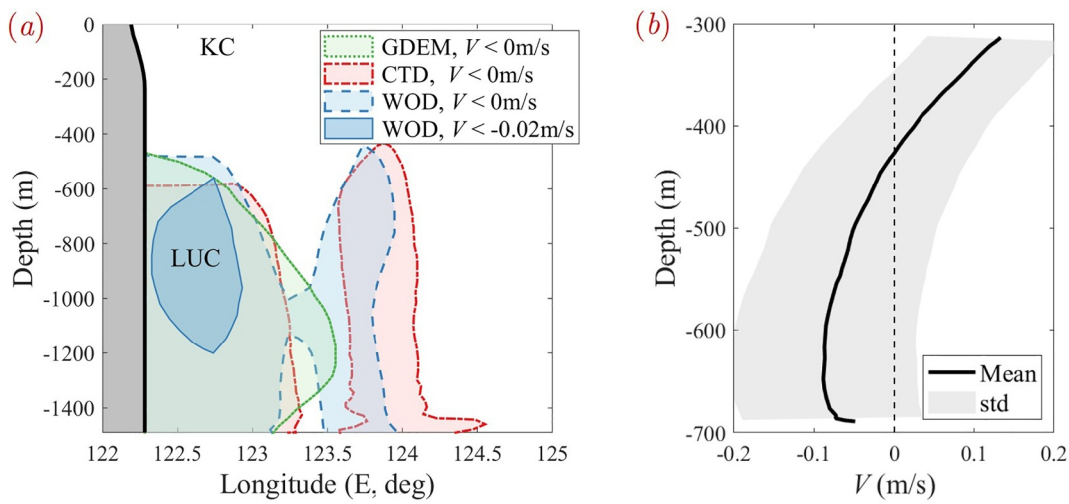

Figure 2. (a) Undercurrent region (negative meridional velocity) at 18°N inferred from hydrographic data. Data sources are the global digital elevation model (GDEM, https://lpdaac.usgs.gov/products/astgtmv003/), from Qu et al. (1997) using CTD and from Wang et al. (2015) using the World Ocean Database (WOD09), respectively. (b) The mean meridional velocity and its standard deviation from the direct measurement of Hu et al. (2013) at 18°N, 122.7°E.

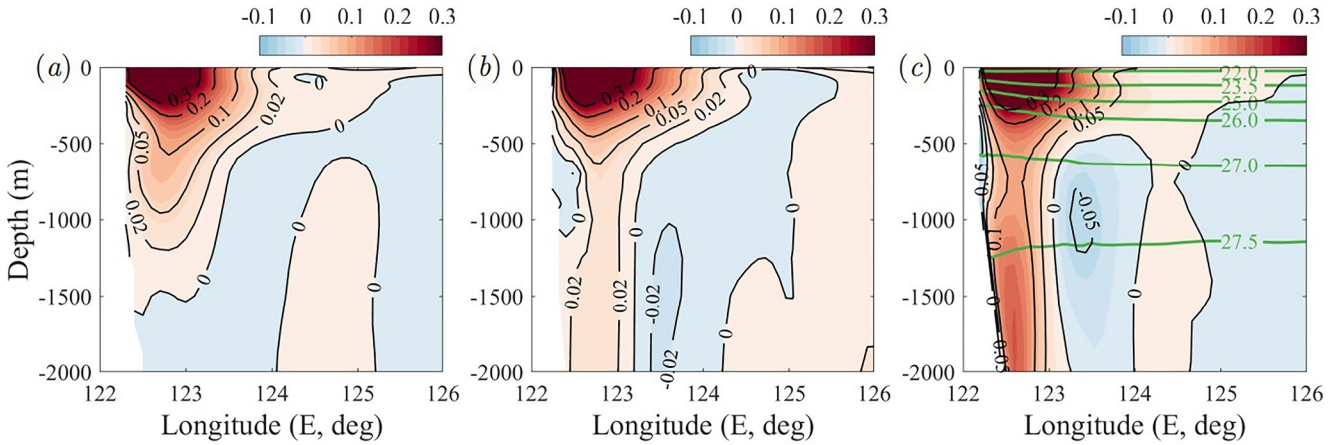

Figure 3. Mean meridional velocity (m/s) at 18°N from (a) OFES (from 1999 to 2009), (b) HYCOM (from 1993 to 2012), and (c) CMOMS (from years 46–50). The green lines represent the potential density (kg/m^3). Note that the CMOMS results in panel (c) were computed without using the modified parameterization to be presented in this study (see Section 2.3).

period of ~70 days, which is regarded to closely relate to the westward eddies east of LI (Hu et al., 2013; Wang et al., 2014). Furthermore, using direct measurement (see Figure 2b), Hu et al. (2013) demonstrated that the maximum velocity of the LUC could exceed 0.275 m/s, and the LUC is stronger in winter and summer (see also Z. Chen et al., 2015; Lien et al., 2015). The notable difference in the maximum velocity between hydrographic data and direct measurements indicates a prominent role of ageostrophic motions for the LUC. Despite lots of progress in revealing the basic features of the LUC, knowledge of the LUC dynamics is still limited. Very recently, Li and Gan (2022a) found, based on the World Ocean Atlas data, that the origin of the LUC is closely connected to the southward veering Deep North Equatorial Current (DNEC) off the Ryukyu Islands and the Luzon Strait middle-layer outflow (LSMO). They also noted that the existence of the LUC is dynamically linked with both barotropic and baroclinic effects.

Besides observations, numerical ocean modelings have been used to investigate the LUC. For example, Gao et al. (2012) implemented water property tracking and suggested that approximately 41% of the LUC water was traceable to the winter mixed layer in the Kuroshio extension, and the rest was trapped in the northern subtropical gyre. Also, diapycnal mixing was significant in converting subtropical waters to the LUC. Nevertheless, few modeling experiments have actually captured the structure of the LUC and explained its dynamics. In fact, we have examined available results from several prevailing regional/global models and found that the results regarding the LUC are somewhat inconsistent with observations. For example, we present in Figure 3 the long-term mean velocity contours at 18°N from three representative global/regional models. The first model is the OFES (https://www.jamstec.go.jp/ofes/ofes.html) using a horizontal resolution of 0.1° and 54 vertical levels. The second one is the HYCOM (https://www.hycom.org/) using a 0.08° horizontal resolution and 40 vertical levels. The third one is the China Sea multi-scale ocean modeling system (CMOMS) using a 10 km horizontal resolution and 30 terrain-following vertical levels (see Section 2.1 for details). The first two models are well known for simulating global ocean circulations (Chassignet and Xu, 2007; Masumoto et al., 2004), and the third model is successful in resolving regional circulation in WPO and southeast Asia marginal seas (Gan, Liu, & Hui, 2016, Gan, Liu, & Liang, 2016). As shown in Figure 3, the KC from these three models seems extending too deep compared to Figure 2. The water deeper than 600 m still flows northward, and the inshore core of the LUC beneath the KC is either too weak or nonexistent. It is suggested that, although these global models have been proven effective for most abyssal regions, they may not be accurate enough to capture the LUC likely due to physically unresolved local complexities. The inconsistency between observations and modelings strongly motivates us to perform this research. Our objective is to reasonably capture the LUC based on physics reasoning and experiments of physically based modeling.

Various factors could lead to the deficiencies between Figures 2 and 3. As an undercurrent, we seek reasons from the dynamic perspective of the LUC, which is still not well understood. As shown in Figure 3c, the isopycnal tilting in this western boundary region is relatively strong, which relates to high vertical shear through the thermal

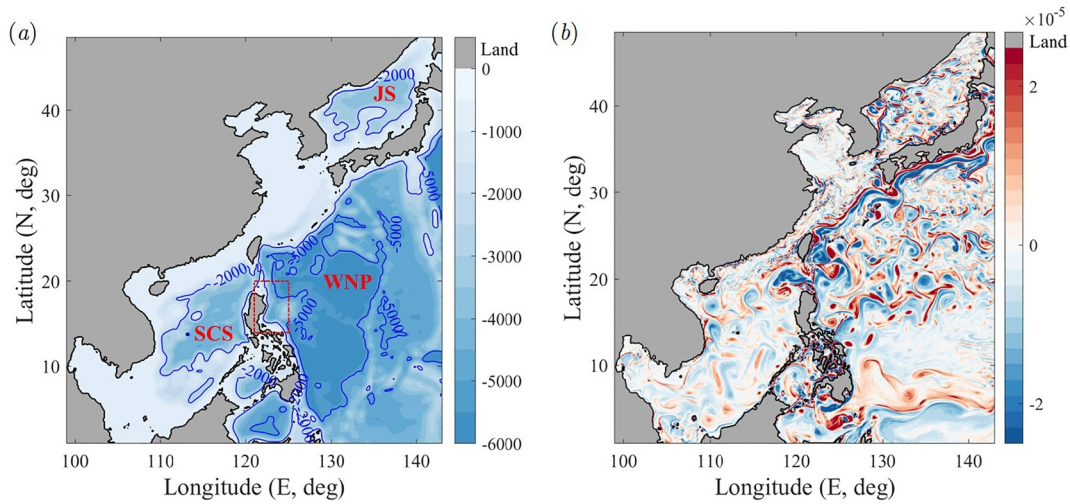

Figure 4. (a) Illustration of the computational domain and contours of bathymetry (m) and (b) the daily-output surface relative vorticity (1/s) (3 km case, June 1st). The box outlined with red dashed lines in panel (a) denotes the region of interest for the KC–LUC system.

wind balance. Therefore, baroclinicity and vertical mixing are expected to be important factors for the LUC dynamics, which were recently explored by the present authors in idealized current-undercurrent models (X. Chen et al., 2023, 2024). The models in Figure 3 utilized prevailing vertical mixing schemes: the *K*-profile vertical parameterization (KPP; Large et al., 1994) for OFES and HYCOM and the M–Y scheme (Mellor & Yamada, 1974, 1982) for CMOMS. These schemes adopt universal parameters so they can be inaccurate when applied to specific regions due to local instability and turbulence (Thorpe, 2007). We will review these vertical mixing parameterizations later in Section 2.3. Moreover, Köhler et al. (2014) showed that the vertical eddy diffusivity in the thermocline can increase from $\sim 10^{-5}$ to $\sim 10^{-3}$ m^2/s near a western boundary. This two orders of magnitude variation can severely affect geostrophic flows and can be a large source of uncertainty regarding current variability. Therefore, inaccurate vertical mixing parameterization can be responsible for the discrepancies between models and observations for the WBCs and WBUCs, which call for more scrutiny on the parameterization. In this work, we explore the LUC dynamics and improve the vertical mixing parameterization for modeling so that we can resolve the current-undercurrent system better and capture the LUC wholly and accurately.

The remainder parts are organized as follows. Section 2 describes the benchmark model and the direction of improvement learned from benchmark results. Section 3 discusses the simulation results and the dynamics of the LUC. Finally, the work is summarized in Section 4.

2. Benchmark Model and a Munk-Like Adaptive Mixing Scheme

2.1. Benchmark Model Results

We use the CMOMS (https://odmp.ust.hk/cmoms/) to unveil the LUC characteristics and underlying physics. CMOMS is built upon the Regional Ocean Modeling System (ROMS; Shchepetkin & McWilliams, 2005), solving the primitive equations to resolve three-dimensional time-dependent circulations. CMOMS has been validated rigorously with available evidence from observations and theoretical justifications (Gan, Liu, & Liang, 2016, 2022; Li & Gan, 2022b).

To resolve the northern WPO with marginal seas, we select a computational domain from 99°E to 143°E and 0.9°N to 48.5°N as illustrated in Figure 4a. We run the climatological benchmark model with two sets of resolutions for inter-case comparison. The coarser resolution is 10 km, and the finer one is 3 km, along with 30 and 60 vertical levels, respectively, in the terrain following coordinate (*s* coordinate; Song & Haidvogel, 1994). The other numerical configurations are detailed in Appendix A, including the horizontal mixing scheme, water depth data, wind forcing, atmospheric fluxes, river discharges, and boundary and initial conditions. The level-2.5 scheme by Mellor and Yamada (1982) is used in the benchmark model.

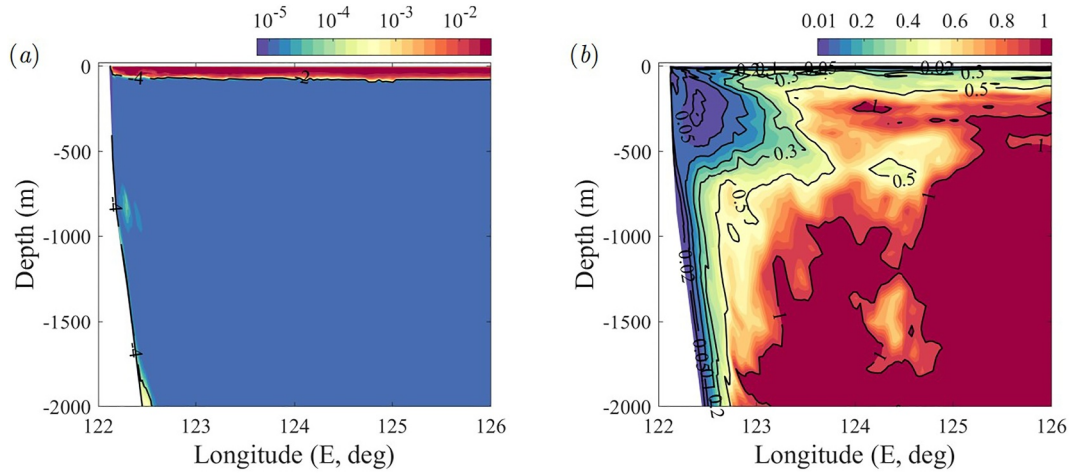

Figure 5. Contours of the (a) vertical eddy diffusivity (m^2/s) and (b) Richardson number in the cross-shore section at 18°N for the benchmark case (annual mean of Year 3).

Figure 4b displays the daily-output surface relative vorticity, $\zeta = v_x - u_y$, to demonstrate the high-resolution computation we performed (3 km case). The strong vortical motions in the WPO, SCS, and Japan Sea, especially near the western boundaries, are clearly exhibited. Also, mesoscale eddies are clearly recognized. The model resolved the upper-layer circulations well (see Section 3.1 for more details), and the three-layer circulation in the SCS was revealed (Gan et al., 2022). However, as shown in Figure 3c, the LUC (within the red box in Figure 4a) was not captured correctly at both resolutions. We provide more discussions on the incapability of the benchmark model below in Section 2.2 and suggest possible improvements to the parameterization in Section 2.3.

2.2. Eddy Diffusivity and Richardson Number Scaling

As stated in Section 1, the vertical eddy diffusivity A_{kv} in the thermocline can increase from $\sim 10^{-5}$ m^2/s to $\sim 10^{-3}$ m^2/s near the western boundary (Köhler et al., 2014; Samelson, 1998), so the vertical mixing parameterization can be a large source of uncertainty for current variability. Focusing on the KC and LUC east of LI, we analyzed the vertical mixing in the benchmark results to provide a physical guide for modification.

Figure 5a presents the distribution of the annual mean A_{kv} at 18°N for the benchmark case (Year 3). Following M–Y, A_{kv} is obtained from the equations of eddy fluctuation moments and length scales. In the mixed layer within $\sim$100 m depth, subgrid-scale turbulent motions are highly active, so A_{kv} has a large amplitude $\sim 10^{-2}$ m^2/s. Below the mixed layer, A_{kv} is uniformly low at a background value $\sim 10^{-5}$ m^2/s and remains small toward the western boundary. However, the turbulence in the thermocline is intermittent and episodic, and there can be strong thermocline mixing in specific regions due to, for example, locally enhanced shear instabilities and internal wave breaking (Large et al., 1994). Consequently, the induced thermocline mixing may not be well represented by the original M–Y model. In fact, inadequate mixing in the stably stratified but strongly sheared thermocline/halocline is regarded as one of the major shortcomings of the M–Y model (Kantha & Clayson, 1994).

For further insight into the thermocline vertical mixing for the LUC, we pay special attention to the (gradient) Richardson number

$$Ri = \frac{N^2}{\left(\frac{\partial u}{\partial z}\right)^2 + \left(\frac{\partial v}{\partial z}\right)^2}, \tag{1}$$

where N^2 is the buoyancy frequency, u and v are the zonal and meridional velocities, and z is the vertical coordinate. By definition, Ri measures the ratio of buoyancy gradient to flow shear, so it is crucial in classifying different types of instabilities (Stone, 1970). Also, Ri is closely related to the strength of vertical mixing, a relation first derived by Munk and Anderson (1948) using dimensional analysis. At small Ri ($\lesssim 1$), the high vertical shear and weak stratification can induce strong vertical motions and turbulent diffusion through for example symmetric

and Kelvin-Helmholtz instabilities (Stone, 1970). Theoretical research indeed suggests deficiencies of the M–Y model at small *Ri*. Canuto et al. (2001) showed that several terms in the pressure correlation tensors were neglected in M–Y, which relate to the contribution of buoyancy, shear, and vorticity. This simplification can lead to an underestimation of the critical *Ri* (suggests the occurrence of instability), from ∼1 to 0.2, for idealized flows, which means that the vertical mixing at $Ri \lesssim 1$ can be underestimated in the M–Y model.

Figure 5b shows the distribution of *Ri* for the same region as in Figure 5a. In the mixed layer, *Ri* in the benchmark model is small because the thermal field is well mixed. In the offshore thermocline, *Ri* is of order one; close to the western boundary, however, *Ri* in the thermocline decreases to ∼0.02, indicating enhanced vertical shear and intensified vertical mixing. As seen in Figure 3c, the water beneath the KC keeps flowing northward, so it can be conjectured that the vertical shear, though enhanced, is still smaller than required when the LUC is present. Based on the thermal wind relation, the vertical shear needs to be balanced by horizontal buoyancy gradient or equivalently the isopycnal tilting. To sustain this tilting, a thick thermocline is required near the western boundary, which corresponds to large A_{kv}. Thereby, based on Figure 5 and the deficiencies of the M–Y model at small *Ri* discussed above, we speculate that the benchmark model underestimates the thermocline vertical mixing for the highly sheared current-undercurrent system near the western boundary. We further hypothesize that this underestimated mixing undermines local baroclinic dynamics and, thus, geostrophic support for the LUC, leading to unresolved inshore LUC core beneath the KC. In the following, we present a posteriori analysis to support this hypothesis. We modify the mixing parameterization for enhanced thermocline vertical mixing near the western boundary. We will demonstrate that the LUC can be captured reasonably after adopting the modification and prove the self-consistency of the hypothesis through analyzing the LUC dynamics.

2.3. Vertical Mixing and a Munk-Like Adaptive Scheme

The mixing parameterization has been a hot topic of research in geophysical fluid dynamics for several decades (see, e.g. the summaries of Large et al., 1994; Fox-Kemper et al., 2022). The characteristic scales of turbulent motions (∼cm, Thorpe, 2007) are far less than the grid sizes adopted for global/regional models, so parameterizing subgrid-scale mixing is indispensable and can be a large source of uncertainty due to unresolved physics of turbulence. Various modeling approaches have been developed to parameterize the vertical mixing within and below the surface mixed layer, among which diffusion models are prevailing. Moreover, the diffusion models can be classified into two types, namely the first- and second-moment closure models.

The first-moment closure model is built upon abundant theoretical and observational knowledge of fluid motions and contains empirical or semiempirical relations (D. Chen et al., 1994). The eddy-induced transport of heat, salinity, and so on in the interior flow is modeled as

$$-\overline{w'T'} \sim A_{kv,T}\frac{\partial T}{\partial z}, \qquad -\overline{w'S'} \sim A_{kv,S}\frac{\partial S}{\partial z}, \tag{2}$$

where w is the vertical velocity, and the prime stands for eddy-induced components. The eddy diffusivities $A_{kv,T}$ and $A_{kv,S}$ can be related to momentum diffusion through Prandtl numbers. The eddy diffusivities are usually separately formulated within and below the mixed layer to interpret different physics. In the mixed layer, there can be additional nonlocal terms to represent turbulent nonlocal transport (Large et al., 1994). Below the mixed layer, vertical mixing can be dominated by shear instabilities, so its strength connects with local *Ri*, which expresses the relative importance of vertical shear and stratification. Using dimensional analysis, Munk and Anderson (1948) suggested that A_{kv} is a function of *Ri*, namely $A_{kv} = A_{kv}(Ri)$. This relation has been verified, for example, Peters et al. (1988), using observational data. As a result, the form $A_{kv}(Ri)$ has been extensively adopted to parameterize shear-induced mixing and distinguished from those induced by internal wave breaking, double diffusion, and others. Different functions have been proposed based on physics reasoning and curve fitting (Jones, 1973; Large et al., 1994; Pacanowski & Philander, 1981). The specific expressions of these schemes will be described later. A basic physical guideline is that A_{kv} increases monotonically as *Ri* decreases ($Ri > 0$).

In comparison, the second-moment closure models are primarily designed for the turbulent mixed layer. They are derived by appealing to a closure of turbulence quantities at the second (or higher) moment. Therefore, additional equations are required to describe eddy-induced quantities like the eddy kinetic and potential energies (Galperin et al., 1988; Mellor & Yamada, 1974, 1982). The second-moment closure model is classified into different levels

according to the number of independent variables and simplifications introduced. The level-2.5 model additionally solves the equation of eddy kinetic energy and other simplified moment equations and is one of the most used models within this branch owing to its balance between accuracy and cost.

Despite their wide success, it is generally recognized that neither the first- nor the second-moment closure schemes are universal and robust enough to be globally accurate over various configurations due to high sensitivities of turbulence and intermittent motions to flow conditions (Thorpe, 2007). For the first-moment closure schemes, it is challenging to find out a single set of parameters that can be applied for various conditions over global oceans (Durski et al., 2004; Jackson et al., 2008; Peters et al., 1988). For example, Durski et al. (2004) commented that KPP can be problematic in coastal oceans, especially where the surface and bottom layers interact heavily. On the other hand, the level-2.5 model tends to provide inadequate mixing in a stably stratified but strongly sheared thermocline/halocline with $Ri \lesssim 1$ (Canuto et al., 2001; Ezer, 2000; Kantha & Clayson, 1994). In short, the first-moment model tends to perform better in the interior of open oceans and in strongly sheared areas, but it can behave poorly in coastal regions. In comparison, the second-moment model performs better in coastal or low shear (high Ri) regions, but it tends to underestimate the interior mixing. Therefore, some combination of the two models can be a good choice to make use of their respective advantages. For example, Kantha and Clayson (1994) used the level-2.5 model and particularly enhanced the thermocline mixing by adding the $A_{kv}(Ri)$ of the interior KPP. Similarly, D. Chen et al. (1994) designed a hybrid vertical mixing scheme based jointly on the Kraus-Turner-type mixed-layer model and Price's dynamical instability model. These novel combinations inspire us to modify the benchmark mixing parameterization using similar strategies.

As stated in Section 2.1, our benchmark model used the M–Y scheme, which was successful in simulating the SCS with large portion of coastal shelf (Gan et al., 2022). The A_{kv} in the benchmark scheme is calculated as

$$A_{kv} = A_{kv,\mathrm{MY}} + A_{kv,\mathrm{bak}}, \tag{3}$$

where $A_{kv,\mathrm{MY}}$ is obtained from stability functions and moment equations, and $A_{kv,\mathrm{bak}}$ is a background value accounting for internal wave breaking. A common choice is $A_{kv,\mathrm{bak}} \approx 10^{-5}$ m^2/s (e.g., Large et al., 1994) as shown in Figure 5a. Meanwhile, the eddy diffusivity and eddy viscosity are related through the balance of the second-order moments. The ratio of eddy diffusivity to eddy viscosity can be high ($\gg 1$) in regions of small Ri.

As discussed in Section 2.2, the benchmark scheme underestimates the thermocline vertical mixing for small Ri ($\lesssim 1$). To compensate for this underprediction and avoid smearing the upper-layer circulation, we employ instead the first-moment closure scheme $A_{kv,s}$ below the mixed layer (below ~100 m) to represent the mixing induced by shear instabilities, as

$$A_{kv} = A_{kv,s} + A_{kv,\mathrm{bak}}, \tag{4}$$

where $A_{kv,s}$ is a function of Ri. Therefore, the present scheme is a merged or hybrid one, a similar thought as considered by Kantha and Clayson (1994) and D. Chen et al. (1994), which aims to combine the respective advantages of the first- and second-moment models.

Next, we consider the specific form of $A_{kv,s}(Ri)$. The KPP interior scheme is prevailing, so we have considered directly substituting $A_{kv,s}$ with KPP, but the LUC is not well resolved, which is also reflected in the OFES and HYCOM results in Figure 3. Therefore, we turn to consider the classical Munk-like schemes as alternatives (Munk & Anderson, 1948), which are also widely used (e.g., Jones, 1973; Monin & Yaglom, 1971; Pacanowski & Philander, 1981; Peters et al., 1988; Yu & Schopf, 1997) and allow more flexible parameterization to reflect local flow complexity. The Munk-like scheme takes the form of

$$A_{kv,s} = \frac{K_{\max}}{(1+\gamma Ri)^{\alpha}}, \tag{5}$$

where $K_{\max}$ is the maximum eddy diffusivity (at $Ri = 0$), and α and γ are fitting coefficients with common ranges between -1 to 10 and -2 to 1.5, respectively (Jones, 1973; Pacanowski & Philander, 1981). We have examined a wide range of α and γ values, and the optimal values are determined to be $\alpha = -3.5$ and $\gamma = 1.5$ for our problem as will be discussed in Section 3. Meanwhile, $K_{\max}$ in Equation 5 is set to 5×10^{-3} m^2/s, following Samelson (1998)

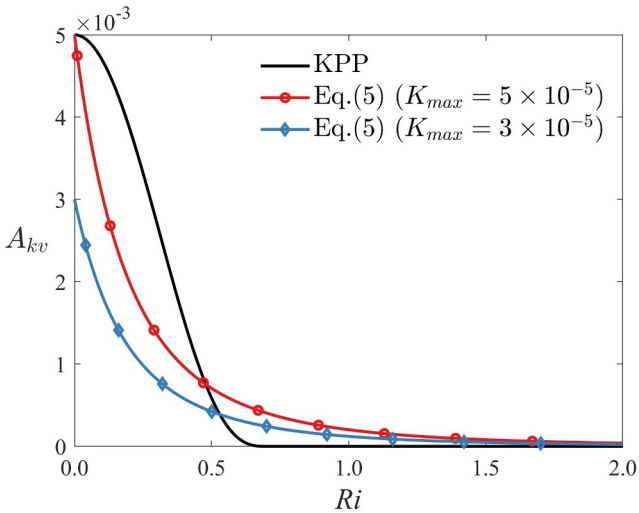

Figure 6. Distribution of the vertical eddy diffusivity coefficient (m^2/s) with the Richardson number from the KPP interior scheme and Equation 5 with different K_{max}.

and Köhler et al. (2014). For demonstration, $A_{kv,s}$ with different K_{max} are depicted in Figure 6, along with the KPP interior scheme. The A_{kv} of KPP remains negligible at large *Ri* and rapidly increases when $Ri < 0.6$, reaching a maximum 5×10^{-3} m^2/s with *Ri* approaching zero. Our experiments within the benchmark model show that the KPP tends to overestimate A_{kv} when $Ri < 0.6$, which distorts the upper-layer NKM circulation. In comparison, the A_{kv} from Equation 5 is lower at $Ri < 0.5$ and rises at an increasing rate when *Ri* tends to zero (convex function), which was supported by observational measurements (Peters et al., 1988) that the eddy diffusivities have steep slopes as *Ri* approaches zero. Hence, the Munk-like scheme emphasizes more the vertical mixing in regions of high shear and weak stratification, such as WBCs and WBUCs. The effect of this design will be exhibited in Section 3.

In short, by combining Equations 3–5, we have designed an adaptive mixing scheme (AMS), so the circulation results in the upper layer are maintained, and those in the middle layer can be improved. We emphasize that the AMS is built upon the theoretical work of Munk and Anderson (1948) and is a hybrid scheme combining the respective advantages of the first- and second-moment closure models. The AMS is a viable alternative supplement to KPP and M–Y and can self-adjust (hence "adaptive") to compensate for the missing flow features according to local shear and stratification (Section 2.2).

3. Results and Discussions

In this section, we focus on the results after adopting the AMS. The other configurations of the benchmark model remain unaltered. We will demonstrate that the model well captures the WPO two-layer circulations, especially LUC, and will discuss its basic features and dynamics.

3.1. Results Overview

First, we present an overview of the circulation results. Figure 7 gives a three-dimensional view of the WPO circulation from the 3 km case. The annual mean results in Year 3 are shown, when the simulation enters a quasi-static state. For better illustration of the circulations, we split the domain vertically into two layers to manifest their distinct features. The depth for the split is selected to be 600 m, suggested by previous works (as in Figure 2). The general picture of the simulated NKM (Figure 7a) and NKMU (Figure 7b) is consistent with those described in Section 1. In the upper layer (averaged from 0 to 600 m), the wide westward NEC is located from ~8°N to 18°N. It bifurcates at ~15°N, east of the Philippine Islands, into the northward KC and the southward MC. More importantly, in the middle layer (from 600 to 1,500 m), the model captures the LUC, along with the NEUC, MUC, DNEC, DKC and LSMO. The LUC and MUC are shown to flow along the coastlines and at relatively large speeds >0.1 m/s. They converge at about 13°N to feed the eastward NEUC jets, which are consistent with the observations by Qiu et al. (2013) and Wang et al. (2015). In addition, the LSMO and DNEC have important connection to the LUC that they two directly fed the latter (Li & Gan, 2022a). This connection is also observed in Figure 7b, where the LUC starts at around 19°N near LI. In this sense, the LUC is significant to the subsurface water exchange between the WPO and SCS. More quantitative analyses on the transport and variability of these currents for the CMOMS results can be found by Li and Gan (2022b).

For a clearer view of the LUC structure, Figure 8 depicts the cross-shore sections of meridional velocity at different latitudes (from 19°N to 16°N) along the east coast of LI. The southward LUC appears beneath the KC and attached inshore from 19°N to 17°N, consistent with the observations in Figure 2. At 16°N, the KC has deep intrusions to separate the LUC from the coast due to the hump of LI at 17°N to 16°N. A major part of the KC becomes trapped ~200 km off the coast and above the isopycnal of potential density $\sigma_\theta = 27$ kg/m^3. Below this isopycnal, the inshore LUC extends from the bottom of the KC (~500 m) to deeper than 1,500 m. The velocity peak of the LUC is located between 650 and 850 m at different latitudes as marked in Figure 8. The maximum speed of the LUC exceeds 0.15 m/s, which is also in line with recent direct measurements (Hu et al., 2013; Lien et al., 2015). For more quantitative examination, the mean velocity profile at 18°N is compared with Hu et al. (2013) in Figure 8b2. Their measurement lasted from November 2010 to July 2011 at 122.7°E, and our

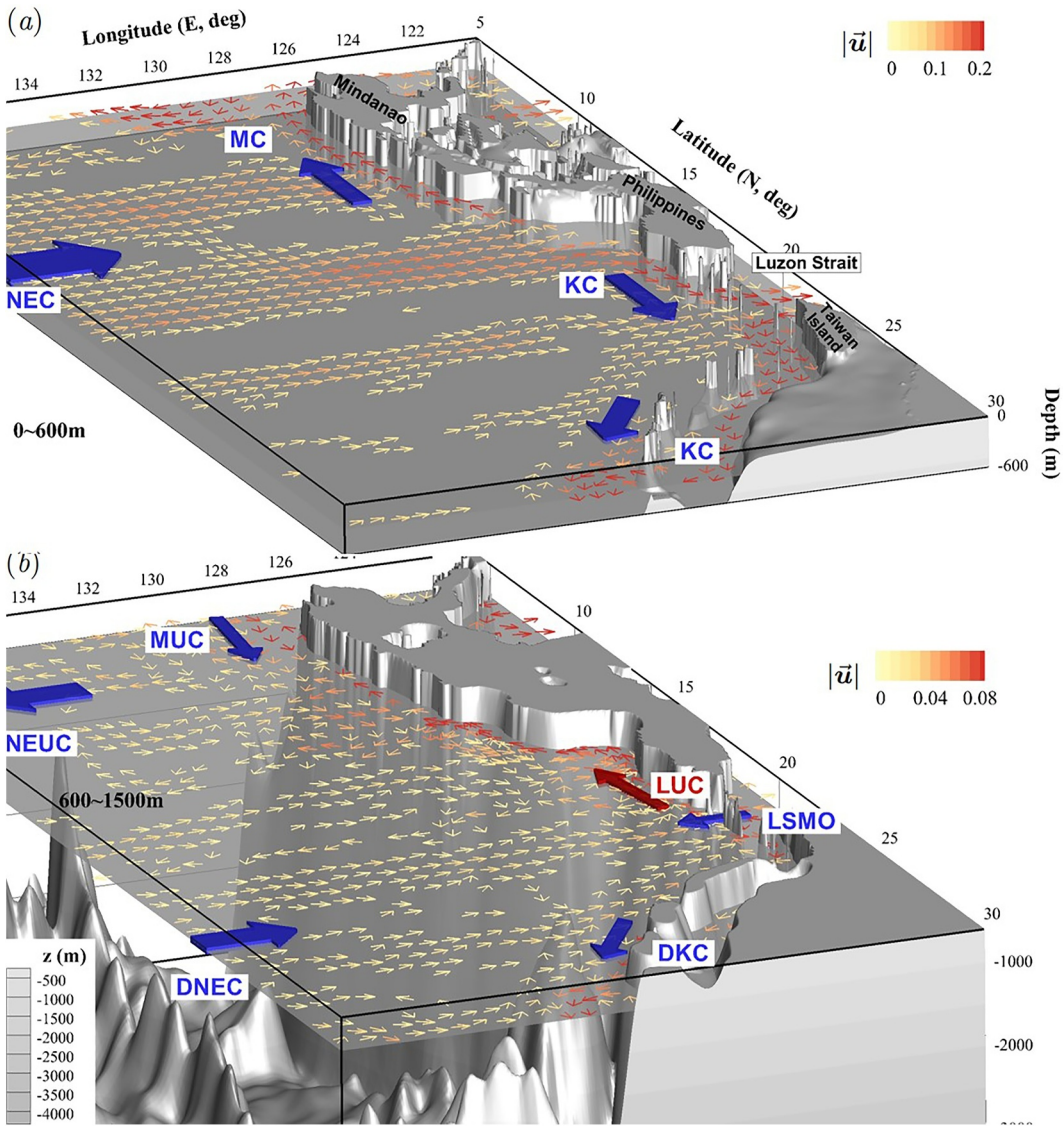

Figure 7. 3D view of the annual-mean velocity (3 km case) in WPO with the AMS in the (a) upper and (b) middle layers. In the upper layer, the horizontal section is at 300 m, showing the velocity arrows averaged from 0 to 600 m. In the middle layer, the section is at 1,000 m with the velocity averaged from 600 to 1,500 m. Abbreviations repeated here as NEC/NEUC, North Equatorial Current/Undercurrent; KC: Kuroshio Current; MC/MUC: Mindanao Current/Undercurrent; DNEC, Deep NEC; DKC, Deep KC; LSMO, Luzon Strait Middle-layer Outflow.

climatological data uses the same span of 7.5 months. The present LUC matches the measurement in terms of strength though at a bit deeper location.

Seasonal variability is another important feature of the LUC, so we plot in Figure 9 the meridional velocity sections at 18°N in different seasons. Here, note that the four seasons are defined as spring (March to May), summer (June to August), autumn (September to November), and winter (December, January, and February). The LUC appears stronger in winter and summer and weaker in spring and autumn, whose phase is well consistent with the trend reported by Hu et al. (2013).

3.2. Dynamics of the LUC

The momentum balance analysis is conducted to further explore the underlying dynamics of the LUC. The momentum equations are written as

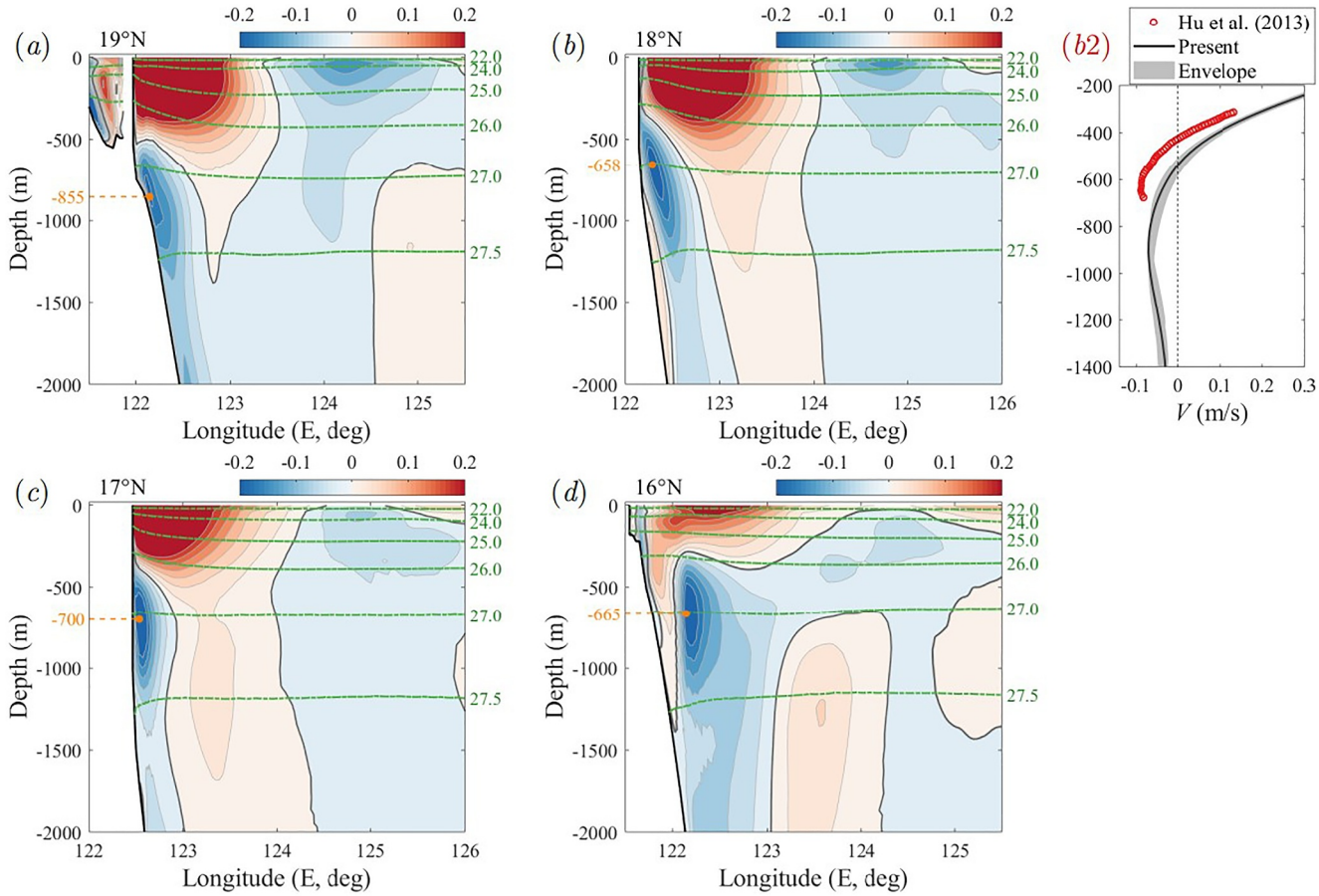

Figure 8. Cross-shore sections of the annual-mean meridional velocity (m/s) using the AMS at (a) 19°N, (b) 18°N, (c) 17°N, and (d) 16°N. The green lines denote the isopycnals as labeled on the right. The orange circles denote the peak location of the LUC velocity amplitudes. Panel (b2) is the mean velocity profile averaged within 122.4°E–123.0°E, where the shades are the envelope of the means at 122.7°E and within 122.6°E–122.8°E, 122.5°E–122.9°E, 122.4°E–123.0°E and 122.3°E–123.1°E; the measurement is from Hu et al. (2013) at 18°N, 122.7°E.

$$\left.\begin{aligned} \overbrace{\frac{\partial u}{\partial t}}^{x-\mathrm{ACC}} + \overbrace{\left(u\frac{\partial u}{\partial x}+v\frac{\partial u}{\partial y}+w\frac{\partial u}{\partial z}\right)}^{x-\mathrm{ADV}} \overbrace{-fv}^{x-\mathrm{COR}} &= -\overbrace{\frac{1}{\rho}\frac{\partial p}{\partial x}}^{x-\mathrm{PGF}} + \overbrace{\nu_h\Delta_h u+\nu_v\frac{\partial^2 u}{\partial z^2}}^{x-\mathrm{VIS}} \\ \underbrace{\frac{\partial v}{\partial t}}_{y-\mathrm{ACC}} + \underbrace{\left(u\frac{\partial v}{\partial x}+v\frac{\partial v}{\partial y}+w\frac{\partial v}{\partial z}\right)}_{y-\mathrm{ADV}} + \underbrace{fu}_{y-\mathrm{COR}} &= -\underbrace{\frac{1}{\rho}\frac{\partial p}{\partial y}}_{y-\mathrm{PGF}} + \underbrace{\nu_h\Delta_h v+\nu_v\frac{\partial^2 v}{\partial z^2}}_{y-\mathrm{VIS}} \end{aligned}\right\} \quad (6)$$

where f is the Coriolis frequency, ν_h and ν_v are the total horizonal and vertical viscosity, and Δ_h is the horizontal Laplace operator. The terms in Equation 6 are classified, as labeled, into the acceleration (ACC), advection (ADV), Coriolis force (COR), pressure gradient force (PGF), and viscous (VIS) terms, respectively. Notably, the derivation and integration of the variables for these terms are treated carefully and implicitly in the CMOMS to ensure that the sum of all terms cancels out (Cai & Gan, 2021). COR and PGF determine the geostrophic flow, so we define the collection of others, that is the sum of ACC, ADV, and VIS, as AGE to represent the contribution of ageostrophic motions. Moreover, PGF comprises barotropic (BT) and baroclinic (BC) parts. The former part, denoted as BT-PGF, is contributed by the horizontal gradient of sea surface height, whereas the latter part (BC-PGF) is due to nonparallel isobaric and isopycnal surfaces. These two parts are computed separately because Section 2.2 suggests that the BC components are crucial for undercurrents.

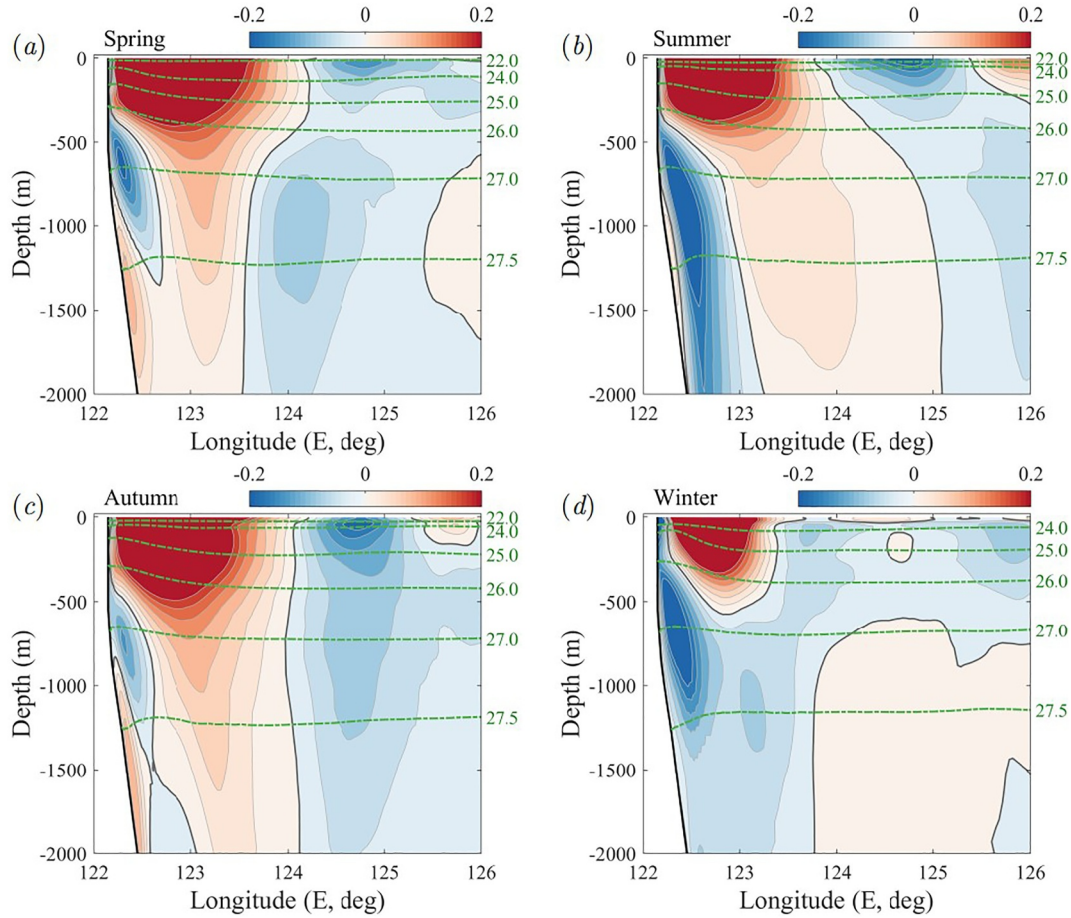

Figure 9. Cross-shore sections of the seasonal mean meridional velocity (m/s) using the AMS at 18°N: (a) spring, (b) summer, (c) autumn, and (d) winter. The green lines denote the isopycnals as labeled on the right.

We focus on the region 120°E–128°E and 13°N–23°N. The horizontal distributions of different terms are plotted in Figure 10 to show their horizontal connection. The two depths displayed are 10 and 700 m around the locations of the strongest KC and LUC, respectively. The distribution of x-PGF is nearly the same as x-COR with an opposite sign (thus not shown), indicative of a rough geostrophic state for large-scale circulations. Nevertheless, both x-AGE and y-AGE have large amplitudes in LS and west of Philippine Islands, and the two are dominated by ADV (advection). From Figure 7, LS is a region where different currents from WPO and SCS strongly interact, so the exchange of momentum at different scales severely enhances ageostrophic motions. Similarly, the presence of LI forces the bifurcation of the NEC, which induces mesoscale and even submesoscale eddies. When down to 700 m, x-PGF in Figure 10d becomes positive on the west of LI, leading geostrophically to the southward LUC. The difference between Figures 10a and 10d is mainly caused by x-BC-PGF, so the LUC is primarily sustained by the significant tilting of isopycnals as shown in Figure 8. From Figures 10e and 10f, x- and y-AGE are also strong in LS and near the west coast of LI. These two terms are dominated by ADV, and the same reason as for Figures 10b and 10c holds here. Therefore, baroclinicity and nonlinearity are crucial to the dynamic formation of the LUC.

The vertical structures of the PGF components are displayed in Figure 11 at 18°N from which the dynamics of the KC and LUC can be explained as follows. The westward flow (from the NEC) in the upper layer bifurcates near the coast, forming a negative x-PGF that keeps the northward KC ($-fv$) (Figure 11a). Conversely, a positive x-PGF keeps the southward LUC (Figure 11b). Meanwhile, the lifted isohalines and isopycnals near the coast (Figure 8b) form positive x-BC-PGF and offset x-BT-PGF (Figures 11c and 11d) to finally sustain the LUC. A similar formation mechanism for the MUC was reported by Qu et al. (2012). Figure 11c shows that x-BT-PGF reaches -4×10^{-5} m/s^2 at 122.5°E throughout the water column. The large x-BT-PGF (in amplitude) driving the

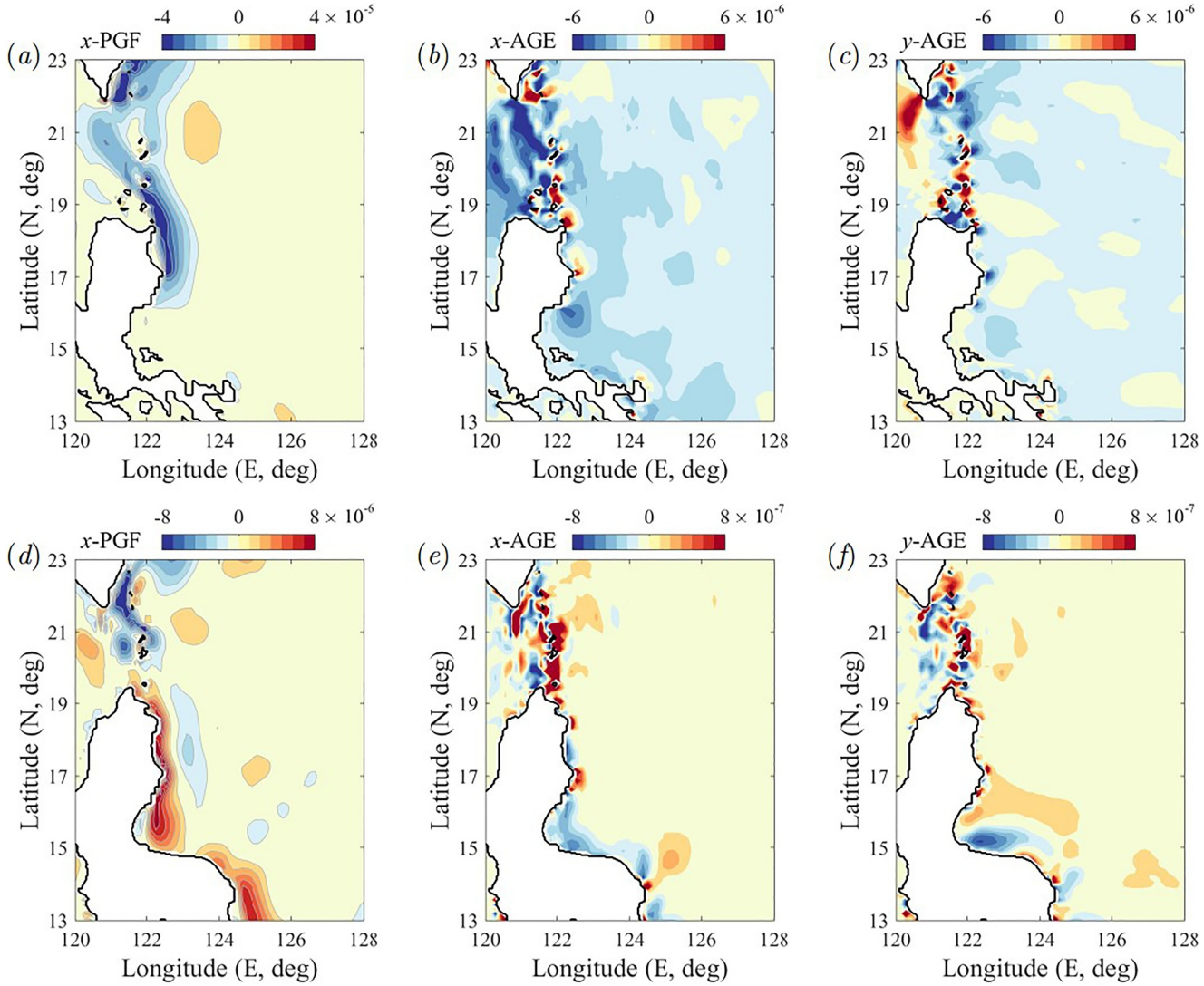

Figure 10. Horizontal sections of different terms in the momentum equations (annual mean): (a, d) pressure gradient force, (b, e) ageostrophic term in the *x*-momentum equation, and (c, f) ageostrophic term in the *y*-momentum equation. (a, b, c) is at depth 10 m and (d, e, f) is at 700 m. Positive and negative values in panels (a, d) refer to eastward and westward *x*-PGF, respectively.

KC also presses the water below the KC to flow northward. In contrast, the strong isopycnal tilting generates high *x*-BC-PGF (Figure 11d) near the coast to balance *x*-BT-PGF. *x*-BC-PGF varies more rapidly in the horizontal direction than the vertical. Its maximum also exceeds 4×10^{-5} m/s^2 and finally drives the subsurface water southward. This strong tilting is related to the high vertical shear in such a current-undercurrent system. However, to sustain this system, enhanced vertical mixing and thus a thick thermocline are required near the western boundary, which is realized by applying the modified parameterization.

It is also worth mentioning that in a current-undercurrent system with strong baroclinicity, various types of geostrophic and ageostrophic instabilities are present (X. Chen et al., 2023, 2024; Molemaker et al., 2005), leading to intensified vertical and ageostrophic motions. This is consistent with the observations in Figure 10 that relatively high AGE exists in the KC–LUC region. Moreover, such pronounced instabilities can partly explain the enhanced vertical mixing in the presence of undercurrents.

In addition to the locally generated dynamics that sustain the LUC, the undercurrent is also linked with upstream remote currents. This remote influx is examined by the southward propagation of PGF. We display the time series of *x*-PGF and *x*-COR in Figure 12 as a function of meridional distance. The region covered is from 20°N to 15°N,

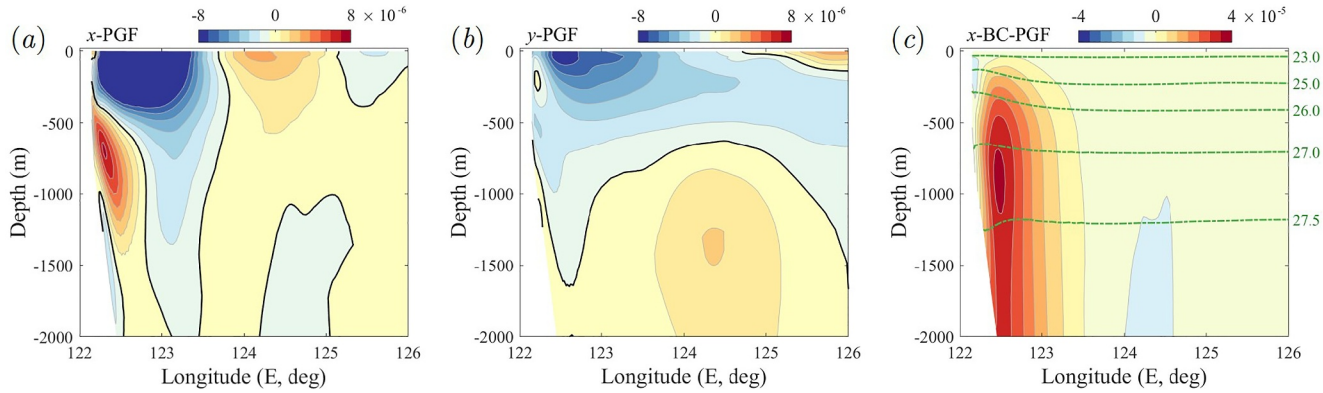

Figure 11. Cross-shore sections of the pressure gradient force in the momentum equations at 18°N (annual mean): (a) *x*-PGF, (b) *y*-PGF, and (c) *x*-BC-PGF. The green lines in panel (c) denote the isopycnals as labeled on the right.

and the quantity plotted is spatially averaged from 122°E to 123°E (land excluded) and 600–1,500 m. A clear trend is observed that both *x*-PGF and *x*-COR propagate southward in line with the LUC. The first peak cycle starts in December at 20°N and ends in March at 15°N, which corresponds to the strong LUC in winter. Likewise, the second cycle endures from June (20°N) to September (15°N) as a reflection of the relatively strong LUC in summer. Therefore, we confirm the southward propagation of the meridionally correlated geostrophy of the LUC as found by Li and Gan (2022a).

3.3. Effects of the Modified Mixing Scheme

The above analysis demonstrates that the LUC is locally set up and sustained by the enhanced baroclinicity near the western boundary. The strong vertical shear and enhanced nonlinear advection both contribute to the large eddy diffusivity there as modified by the AMS. For further evidence of the benefits of the AMS, *Ri* and A_{kv} using the AMS are demonstrated and compared with the benchmark results (without AMS).

In a similar style to Figure 5, the contours of A_{kv} and *Ri* with AMS are depicted in Figure 13 at 18°N. As a result of Equation 5, A_{kv} in the thermocline is designed to increase in a manner negatively correlated with *Ri*. Compared with Figure 5a, A_{kv} increases by one to two orders of magnitude in this region as large as $\sim 10^{-3}$ m^2/s near the western boundary. Meanwhile, *Ri* in the thermocline is much lower than that in Figure 5b, especially near the

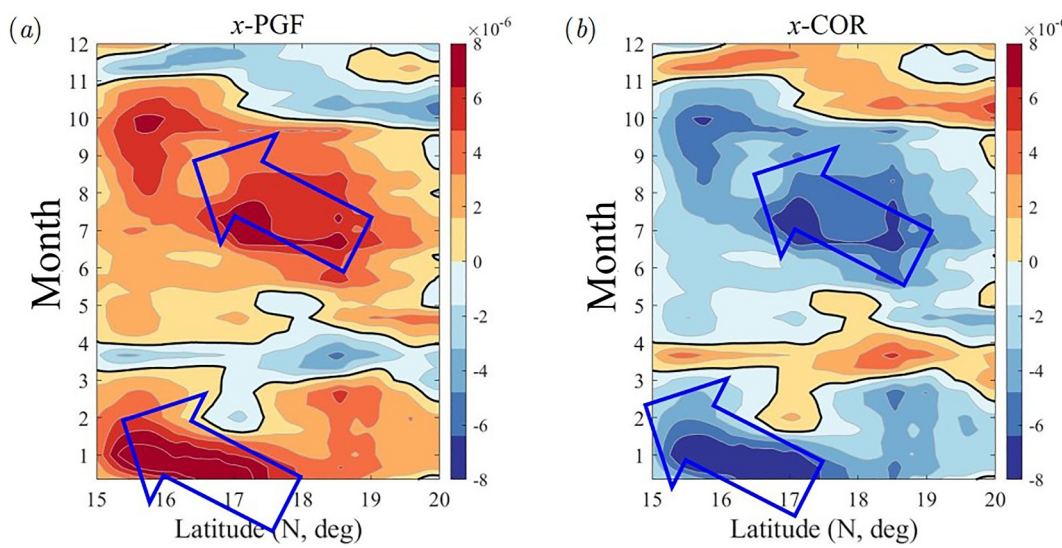

Figure 12. Time series of the (a) pressure gradient force and (b) Coriolis force in the *x*-momentum equation as a function of meridional distance. The terms are spatially averaged within the LUC region. Positive and negative values refer to eastward and westward *x*-PGF, respectively.

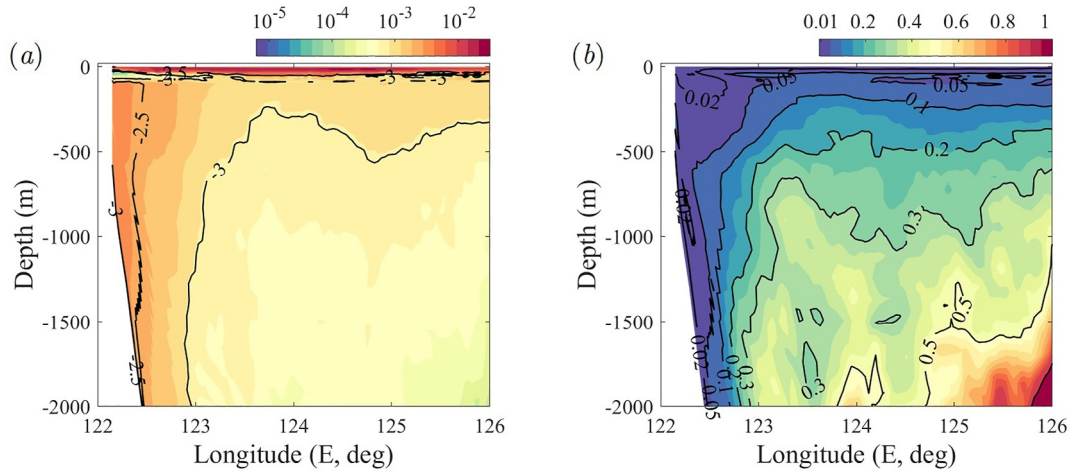

Figure 13. Cross-shore sections of the (a) vertical eddy diffusivity (m^2/s) and (b) Richardson number at 18°N in the AMS case (annual mean).

western boundary where *Ri* is below 0.05 within 2000 m. The decrease of *Ri* can be explained as follows. On the one hand, as the KC–LUC structure is formed, the vertical shear increases as the velocity varies more intensively in the vertical direction. On the other hand, the thermocline becomes thicker due to increased A_{kv}, so N^2 decreases. It is suggested that the increase of A_{kv} has a geostrophic effect, and A_{kv} and *Ri* change in a coupling way that the A_{kv} increase and *Ri* decrease reinforce each other until an equilibrium is reached combining with other processes. Meanwhile, the small *Ri* for the undercurrent suggests large vertical strain there, so in this sense, AMS also compensates, at least partially, for the missing strain-induced dynamics (e.g., J. Zhang et al., 2023; Z. Zhang et al., 2023).

The *Ri*-A_{kv} relations are plotted in Figure 14 in a scattered style for the two cases with AMS and without (i.e., M–Y). Only the points below 100 m are shown to exclude the surface mixed layer. Note that the *Ri* and A_{kv} plotted are both annual mean values, so A_{kv} is lower than the theoretical value of Equation 5 in most *Ri* regimes. In Figure 14a, the points between 100 and 2,000 m have A_{kv} less than 5×10^{-4} m^2/s, though *Ri* can be as low as ~0.01. As discussed in Section 2.2, the benchmark model overestimated *Ri* in the small *Ri* region, leading to insufficient geostrophic support for the LUC. In comparison, A_{kv} in Figure 14b is much higher, reaching 10^{-3} m^2/s to 5×10^{-3} m^2/s when $Ri < 0.3$. For reference, the KPP interior relation is also plotted in Figure 14, which predicts

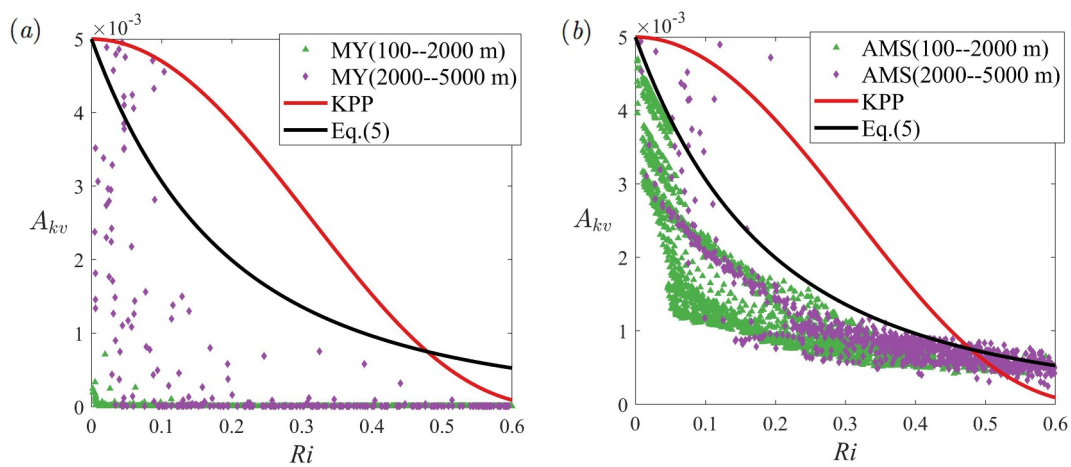

Figure 14. Scatter plot of the eddy diffusivity (m^2/s) and Richardson number from the grid points at specific depth ranges (122°E to 125°E at 18°N; annual mean): (a) no AMS and (b) with AMS. The analytical relations of KPP and Equation 5 are shown for reference.

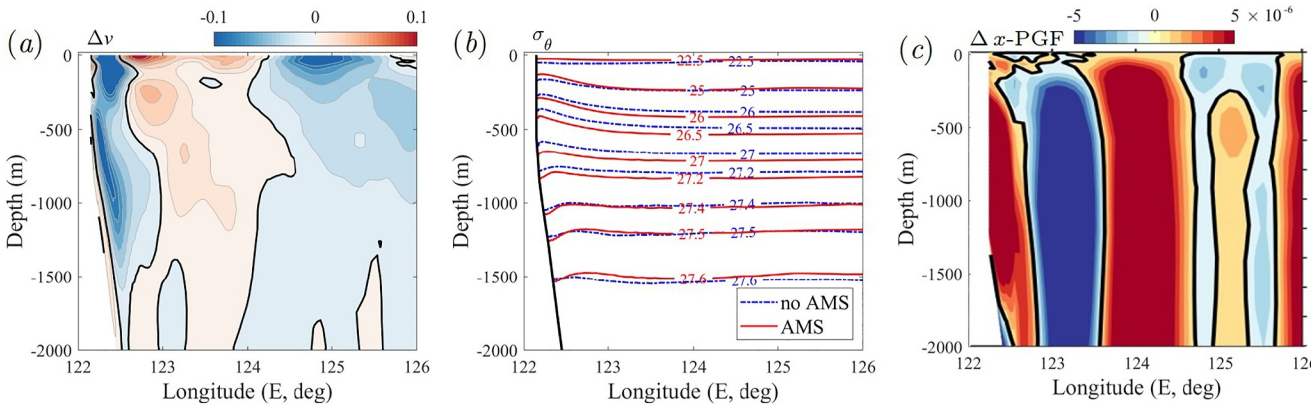

Figure 15. Difference between the results with and without the AMS at 18°N (cross-shore sections, annual mean): (a) meridional velocity (m/s), (b) potential density and (c) pressure gradient force (*x*-momentum). Positive/negative values refer to southward/northward *v*, and eastward/westward *x*-PGF, respectively.

higher A_{kv} when $Ri < 0.4$. We note again that observational measurements (Peters et al., 1988) are indicative of steep slopes for the eddy diffusivities as *Ri* tends to zero, which is reflected in AMS over KPP.

To better demonstrate the effects of the AMS, we study the difference between the two results, calculated as $\Delta\phi = \phi_{\mathrm{AMS}} - \phi_{\mathrm{no-AMS}}$, where ϕ denotes a variable. The differences in meridional velocity, potential density, and momentum budget terms at 18°N are shown in Figure 15. From Figure 15a, the inshore southward flow is considerably strengthened by the AMS, leading to the suppressed KC and enhanced LUC. The maximum velocity difference is over 0.1 m/s southward near the KC and LUC cores. The difference in the velocity is mainly caused by *x*-PGF as shown in Figure 15c. Meanwhile, *x*-PGF varies mildly near the surface and much more heavily in the interior (depth <250 m), so *x*-BC-PGF is altered considerably after using the AMS. Also, Δ(*x*-PGF) experiences a strong horizontal variation. In the very inshore region (~50 km, from 122.5°E to 123.0°E), eastward *x*-PGF and thus southward flow are generated to support the LUC. The region further offshore (from 123.5°E to 124.5°E) is also largely affected, where both eastward and westward *x*-PGF are induced due to the strong isopycnal tilting and thick thermocline in the AMS case as shown in Figure 15b. Moreover, the difference in *x*-AGE (not shown) also bears some resemblance to Δ*v* (Figure 15a) near the western boundary, which indicates that nonlinearity also contributes positively to the enhanced LUC in the AMS case and aligns with Section 3.2 that the pronounced ageostrophic motions are closely related to the intensified baroclinicity. In short, the usage of the AMS in our model better captures the subsurface BC-PGF and thus the geostrophic support for the LUC. Agreement with the analysis in Section 3.2 is obtained, demonstrating the self-consistency in explaining how the LUC is formed and sustained.

3.4. Effects of Submesoscale Motions

Turbulent mixing and baroclinic instability can induce strong submesoscale currents (SMCs; McWilliams, 2016; Zhang, 2024), so the effects of SMCs on the LUC are studied in this subsection. The length scales of SMCs are generally defined as 0.1–10 km in the horizontal, so our 3 km model can partially resolve SMCs as it uses high-order advective schemes. Common indicators of SMCs are the (vorticity) Rossby number $Ro = \zeta/f$ (Figure 4), and the divergence $\nabla \cdot u/f$ (e.g., Lin et al., 2020), so we depict their surface snapshots in Figure 16. In addition to the mesoscale eddies east of LI, there are abundant small-scale vortical motions in LS and along the west coast of LI (Figure 16a) where $|Ro| > 1$. Correspondingly, the currents in LS are highly divergent and thus ageostrophic, which are consistent with the distribution of AGE in Figure 10. Therefore, LS and the west coast of LI are regions with active SMCs.

For further insight into the SMCs or fine-scale (FS) motions, the velocity field is decomposed according to their horizontal length scales using the coarse-graining method by Storer et al. (2022). The mean kinetic energy of FS is computed as a measure of their long-term contribution, so the resulting FS velocity magnitude is:

$$\overline{|u|}_{\mathrm{SMCs}} = \sqrt{\overline{u_{\mathrm{FS}}^2 + v_{\mathrm{FS}}^2}}. \tag{7}$$

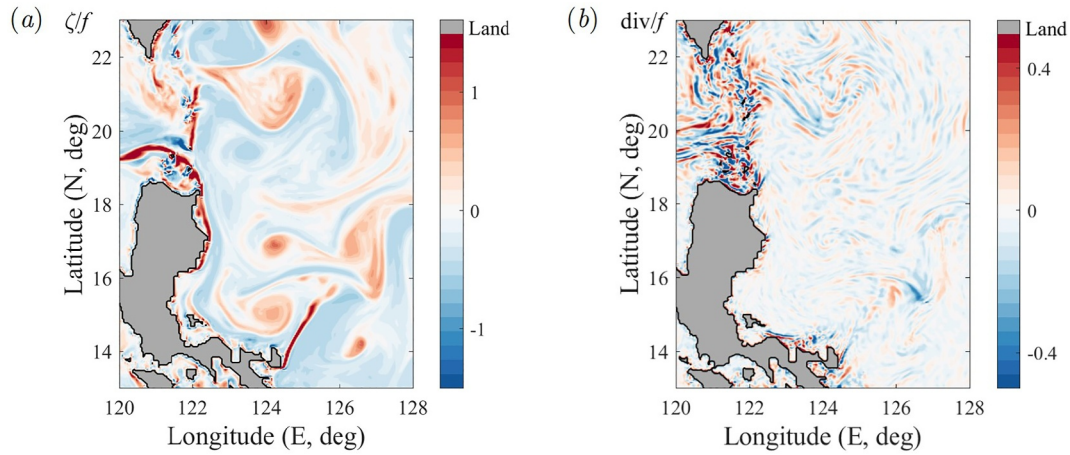

Figure 16. Snapshots of surface (a) Rossby number ($Ro = \zeta/f$) and (b) divergence ($\mathrm{div}/f = \nabla \cdot u/f$) (the AMS case, June 1st).

The annual mean $\overline{|u|}_{\mathrm{SMCs}}$ at 18°N and 19°N is plotted in Figure 17 to show its spatial distribution. In addition to the high amplitude in the surface mixed layer, $\overline{|u|}_{\mathrm{SMCs}}$ is enriched down to 500–1,500 m in the LUC region, whose maximum is comparable to the mean meridional velocity, demonstrating the essential role of SMCs for the LUC. This is also in line with the indication of direct measurements (see Section 1) that strong ageostrophic motions are present in the LUC region, so hydrographic estimation can underestimate the LUC.

The influence of SMCs on the LUC can also be partly demonstrated by comparing between the two model results with 10 and 3 km resolution. Although the difference between the two cases may be contributed by non-SMCs factors such as numerical discretization errors and forcing sampling frequency, we study the inter-case differences to see the trends when SMCs are resolved. Figure 18a depicts the contours of *Ri* in the 10 km case, which is in a similar distribution to the 3 km case in Figure 13b. Nevertheless, *Ri* in the latter case is basically lower in the thermocline, whose difference is more clearly seen in Figure 18b. Therefore, the thermocline vertical mixing in the 3 km case is stronger as a consequence of pronounced SMCs resolved by the finer mesh. The lower *Ri* is accompanied by enhanced vertical shear and suppressed stratification, which reflects stronger KC and LUC. This is demonstrated in Figure 18c showing the meridional velocity difference Δv ($\Delta\phi = \phi_{3\mathrm{km}} - \phi_{10\mathrm{km}}$). The maximum $|\Delta v|$ exceeds 0.1 m/s, suggesting the non-negligible contribution of SMCs. In fact, the SMCs may also more directly enhance mesoscale motions and finally the large-scale structure through inverse energy cascade as revealed by Zhang et al. (2023a, 2023b) for the Southern Ocean. Therefore, the enhanced KC and LUC at 3 km resolution can be a balance between enhanced mesoscale motions due to inverse cascade and stronger vertical

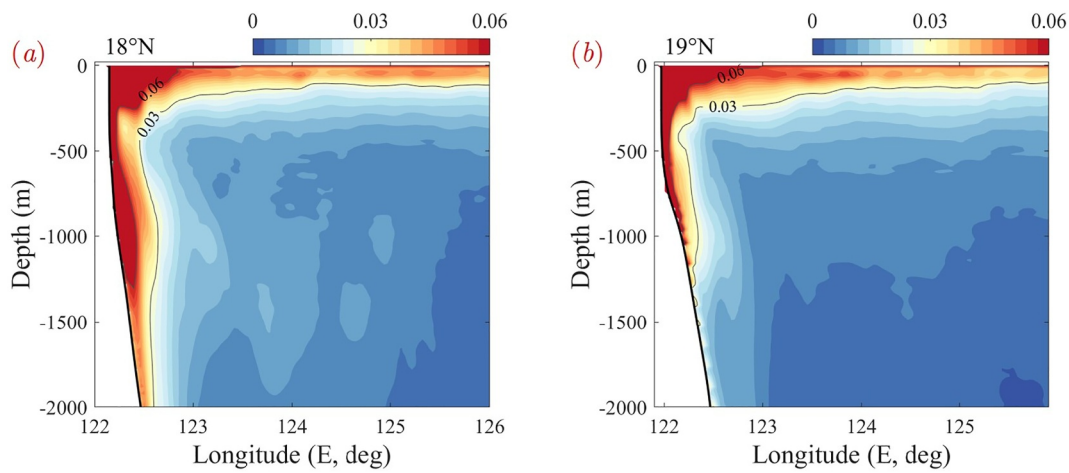

Figure 17. Cross-shore sections of the annual-mean fine-scale velocity magitude (m/s; Equation 7 for the scales <15 km) at (a) 18°N and (b) 19°N.

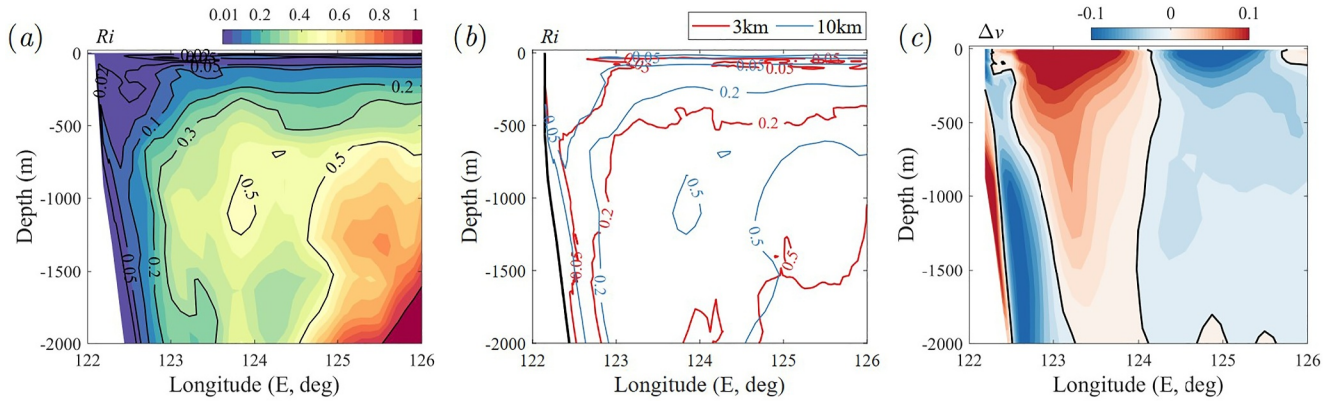

Figure 18. Cross-shore sections of the Richardson number (a) in the 10 km case, and (b) the comparison between the 10 and 3 km cases, and the differences of the (c) meridional velocity (m/s) between the 3 and 10 km cases at 18°N.

mixing due to forward cascade. This point requires further clarification in future works. In short, the SMCs benefit the formation and sustainability of the LUC.

4. Summary

The LUC is one of the most significant WBUCs in the WPO. In the NKMU system, the LUC flows southward to converge with the MUC and then feeds the NEUC jets, hence are important for subsurface water transport and the exchange between subtropical-equatorial circulations. Over the last three decades, abundant observational progress has been made in revealing the basic characteristics of the LUC. However, the LUC had not been reasonably captured in previous numerical simulations (Figure 3). This work intends to improve the modeling results regarding the LUC based on physics reasoning and experiments of physically based modeling, which would also shed light on the dynamics of the LUC.

Particular attention is paid to the vertical mixing, which is sensitive to local complexities of instability and turbulence. Hence, inaccurate vertical mixing parameterization can be responsible for the deficiency in modeling WBCs and WBUCs in the WPO. Based on the benchmark model results and theoretical deficiency of the M–Y model at small *Ri*, we speculate that the thermocline vertical mixing is underestimated for the highly sheared current-undercurrent system, which undermines geostrophic support for the LUC. Therefore, the vertical mixing parameterization is modified for enhanced thermocline mixing for the undercurrent. Specifically, an AMS is designed (Section 2.3), combining the respective advantages of the first- and second-moment closure models. A Munk-like function $A_{kv,s}(Ri)$ is adopted in the thermocline, which can self-adjust (hence "adaptive") to compensate for the undermined vertical mixing at small *Ri* regions. Three-dimensional time-dependent simulation with the AMS scheme is conducted for the WPO and marginal seas using the CMOMS model at a high resolution of 3 km and 60 levels. The WPO circulations for the upper-layer currents and middle-layer undercurrents are reproduced. More importantly, the inshore core of the LUC is reasonably resolved. The location, velocity, and seasonal variability of the LUC are basically consistent with previous measurements, demonstrating the reliability of the present simulation.

The dynamics of the LUC are studied by analyzing the momentum balance. The strong vertical shear for the undercurrent needs to be balanced by the horizontal buoyancy gradient or equivalently the isopycnal tilting. The strong tilting generates large BC-PGF, which is shown to be crucial for the KC–LUC system. To sustain this tilting, a thick thermocline is required near the western boundary, corresponding to large A_{kv} there. Meanwhile, the strong vertical shear and thick thermocline lead to small *Ri* (<0.05) near the western boundary, so the vertical turbulent motions are enhanced and the vertical mixing is strengthened, justifying the introduction of the AMS. Time series of *x*-PGF and *x*-COR demonstrate the southward propagating meridionally correlated geostrophy of the LUC. Furthermore, nonlinear advection terms are pronounced for the KC–LUC system due to the enhanced ageostrophic instabilities at small *Ri*. The effects of nonlinearity are shown to benefit the LUC. Finally, we study the effects of SMCs on the LUC. By computing the Rossby number and the divergence, we show that LS and the west coast of LI are regions with active SMCs. Meanwhile, strong SMCs are observed in the LUC region,

demonstrating their essential roles. Regarding the effects of horizontal resolutions, the thermocline *Ri* in the model of 3 km case is lower than that of the 10 km case, indicating stronger vertical mixing in the high-resolution case. In this sense, SMCs also benefit the formation and sustainability of the LUC. Therefore, nonlinearity, baroclinicity, and SMCs jointly regulate the formation of the geostrophically dominated LUC.

The present work advances the physical understanding of the current-undercurrent system and thus improves the numerical capability in capturing the LUC and WPO circulations. Our findings may also benefit the numerical simulation and dynamics understanding of the current-undercurrent system worldwide.

Appendix A

A1. Computational Configuration

We detail other configurations of the CMOMS computations to complement those already described in Section 2.1. For horizontal mixing, we adopt a Smagorinsky-like scheme for u and v along the s-coordinate surface (Mellor & Blumberg, 1985). Meanwhile, the horizontal eddy diffusivities for T and S are fixed along the isopycnal surface. We obtain the water depths (see Figure 4a) by merging the ETOPO1 data (1/60°) from the NOAA National Geophysical Data Center (2009) with digitized water depths from the navigation maps published by China Maritime Safety Administration (https://www.chart.msa.gov.cn/customer/home). We derive the wind stress that drives the model from the NOAA climatological (averaged from 1988 to 2013) monthly reanalysis of the 10 m blended sea winds with 0.25° × 0.25° resolution (https://www.ncdc.noaa.gov/oa/rsad/air-sea/seawinds.html). To calculate the air-sea interaction boundary layer, we use the atmospheric heat and salt fluxes from the climatological monthly mean NCEP Reanalysis 1 meteorological variables with a resolution of ∼1.875° in the bulk formulation (Fairall et al., 2003). For the lateral buoyancy influxes, we obtain the climatological monthly discharges of the major rivers (Mekong River, Pearl River and Changjiang River) and other minor rivers in the Gulf of Beibu, Bohai Sea, and Yellow Sea from the Information Center of Water Resources (Bureau of Hydrology, Ministry of Water Resources of PR China, http://www.hydroinfo.gov.cn/) and from literature (Dai & Trenberth, 2002). The tidal and subtidal open boundary conditions (TST–OBCs) are used in the lateral eastern and southern boundaries (Liu & Gan, 2016). The local component of the depth-integrated velocities and depth-dependent variables (u, v, T, S) along the open eastern and southern boundaries are derived from the monthly mean solution of the OFES global model (Sasaki et al., 2008) data with a horizontal resolution of 10 km × 10 km. The tidal component of the eight harmonic constituents (M_2, S_2, N_2, K_2, K_1, O_1, P_1, and Q_1) are derived from the TPXO9-alas solution with 1/30° resolution as the tidal boundary forcing (Egbert & Erofeeva, 2002). The initial potential temperature and salinity are obtained from the winter mean solution over the last five years using CMOMS with a horizontal resolution of 10 km × 10 km (Gan, Liu, & Liang, 2016). The temperature and salinity in the bottom layers of the deep basin (depth >200 m) are relaxed to the seasonally averaged values from the WOA13 in 200 days to avoid the drifting of T and S in the deep ocean (Gan et al., 1998). The same relaxation is applied to the upper layer of S in the deep basin to compensate for the uncertainty of the surface salinity flux originating from the NCEP Reanalysis precipitation data.

The model of 10 km horizontal resolution is spun up for 50 years and the model averaged results of the last 5 years are used for the analyses. The model of 3 km horizontal resolution is initialized with the T and S in the 50th year and integrated forward. The steady third year results are used for the analyses.

Data Availability Statement

The data for this study are generated from the publicly distributed Regional Ocean Model System (ROMS; https://www.myroms.org/). The CMOMS data can be found in https://odmp.hkust.edu.hk/cmoms/?page_id=24.

Acknowledgments
This research was supported by the Key Research Project 41930539 of the National Science Foundation, China (NSFC), the Center for Ocean Research in Hong Kong and Macau (CORE), a joint research center between Laoshan Laboratory and Hong Kong University of Science and Technology, the Area of Excellence Scheme (AoE/P-601/23-N), and the Hong Kong Research Grants Council (GRF 16212720).

References

Cai, Z., & Gan, J. (2021). Dynamics of the layered circulation inferred from kinetic energy pathway in the South China Sea. *Journal of Physical Oceanography*, *51*(5), 1671–1685. https://doi.org/10.1175/JPO-D-20-0226.1

Canuto, V. M., Howard, A., Cheng, Y., & Dubovikov, M. S. (2001). Ocean turbulence. Part I: One-point closure model—Momentum and heat vertical diffusivities. *Journal of Physical Oceanography*, *31*(6), 1413–1426. https://doi.org/10.1175/1520-0485(2001)031<1413:OTPIOP>2.0.CO;2

Chassignet, E. P., & Xu, X. (2017). Impact of horizontal resolution (1/12° to 1/50°) on Gulf Stream separation, penetration, and variability. *Journal of Physical Oceanography*, *47*(8), 1999–2021. https://doi.org/10.1175/JPO-D-17-0031.1

Chen, D., Rothstein, L. M., & Busalacchi, A. J. (1994). A hybrid vertical mixing scheme and its application to tropical ocean models. *Journal of Physical Oceanography*, *24*(10), 2156–2179. https://doi.org/10.1175/1520-0485(1994)024<2156:AHVMSA>2.0.CO;2

Chen, X., Gan, J., & McWilliams, J. C. (2023). Biglobal analysis of baroclinic instability in a current–undercurrent oceanic system. *Physical Review Fluids*, *8*(12), 123801. https://doi.org/10.1103/PhysRevFluids.8.123801

Chen, X., Gan, J., & McWilliams, J. C. (2024). Baroclinic nonlinear saturation and secondary instability of current-undercurrent meanders. *Physical Review Fluids*, *9*(10), 103801. https://doi.org/10.1103/physrevfluids.9.103801

Chen, Z., Wu, L., Qiu, B., Li, L., Hu, D., Liu, C., et al. (2015). Strengthening Kuroshio observed at its origin during November 2010 to October 2012. *Journal of Geophysical Research: Oceans*, *120*(4), 2460–2470. https://doi.org/10.1002/2014JC010590

Chern, C.-S., Wang, J., & Wang, D.-P. (1990). The exchange of Kuroshio and East China Sea shelf water. *Journal of Geophysical Research*, *95*(C9), 16017–16023. https://doi.org/10.1029/JC095iC09p16017

Dai, A., & Trenberth, K. E. (2002). Estimates of freshwater discharge from continents: Latitudinal and seasonal variations. *Journal of Hydrometeorology*, *3*(6), 660–687. https://doi.org/10.1175/1525-7541(2002)003<0660:EOFDFC>2.0.CO;2

Durski, S. M., Glenn, S. M., & Haidvogel, D. B. (2004). Vertical mixing schemes in the coastal ocean: Comparison of the level 2.5 Mellor-Yamada scheme with an enhanced version of the K profile parameterization. *Journal of Geophysical Research*, *109*(C1), C01015. https://doi.org/10.1029/2002JC001702

Egbert, G. D., & Erofeeva, S. Y. (2002). Effcient inverse modeling of barotropic ocean tides. *Journal of Atmospheric and Oceanic Technology*, *19*(2), 183–204. https://doi.org/10.1175/1520-0426(2002)019<0183:EIMOBO>2.0.CO;2

Ezer, T. (2000). On the seasonal mixed layer simulated by a basin-scale ocean model and the Mellor-Yamada turbulence scheme. *Journal of Geophysical Research*, *105*(C7), 16843–16855. https://doi.org/10.1029/2000JC900088

Fairall, C. W., Bradley, E. F., Hare, J. E., Grachev, A. A., & Edson, J. B. (2003). Bulk parameterization of air-sea fluxes: Updates and verification for the COARE algorithm. *Journal of Climate*, *16*(4), 571–591. https://doi.org/10.1175/1520-0442(2003)016<0571:BPOASF>2.0.CO;2

Fox-Kemper, B., Johnson, L., & Qiao, F. (2022). Ocean near-surface layers. In *Ocean mixing* (pp. 65–94). Elsevier. Retrieved from https://www.sciencedirect.com/science/article/pii/B9780128215128000116

Galperin, B., Kantha, L. H., Hassid, S., & Rosati, A. (1988). A quasi-equilibrium turbulent energy model for geophysical flows. *Journal of the Atmospheric Sciences*, *45*(1), 55–62. https://doi.org/10.1175/1520-0469(1988)045<0055:AQETEM>2.0.CO;2

Gan, J., Kung, H., Cai, Z., Liu, Z., Hui, C., & Li, J. (2022). Hotspots of the Stokes rotating circulation in a large marginal sea. *Nature Communications*, *13*(1), 2223. https://doi.org/10.1038/s41467-022-29610-z

Gan, J., Liu, Z., & Hui, C. R. (2016). A three-layer alternating spinning circulation in the South China Sea. *Journal of Physical Oceanography*, *46*(8), 2309–2315. https://doi.org/10.1175/JPO-D-16-0044.1

Gan, J., Liu, Z., & Liang, L. (2016). Numerical modeling of intrinsically and extrinsically forced seasonal circulation in the China seas: A kinematic study. *Journal of Geophysical Research: Oceans*, *121*(7), 4697–4715. https://doi.org/10.1002/2016JC011800

Gan, J., Mysak, L. A., & Straub, D. N. (1998). Simulation of the South Atlantic ocean circulation and its seasonal variability. *Journal of Geophysical Research*, *103*(C5), 10241–10251. https://doi.org/10.1029/98JC00367

Gao, S., Qu, T., & Hu, D. (2012). Origin and pathway of the Luzon Undercurrent identified by a simulated adjoint tracer. *Journal of Geophysical Research*, *117*(C5), C05011. https://doi.org/10.1029/2011JC007748

Guo, X., Miyazawa, Y., & Yamagata, T. (2006). The Kuroshio onshore intrusion along the shelf break of the East China Sea: The origin of the Tsushima warm current. *Journal of Physical Oceanography*, *36*(12), 2205–2231. https://doi.org/10.1175/JPO2976.1

Hu, D., & Cui, M. (1989). The western boundary current in the far-western Pacific Ocean. In *Proceedings of western international meeting and workshop on toga coare* (pp. 123–134).

Hu, D., Hu, S., Wu, L., Li, L., Zhang, L., Diao, X., et al. (2013). Direct measurements of the Luzon undercurrent. *Journal of Physical Oceanography*, *43*(7), 1417–1425. https://doi.org/10.1175/JPO-D-12-0165.1

Hu, D., Wang, F., Sprintall, J., Wu, L., Riser, S., Cravatte, S., et al. (2020). Review on observational studies of western tropical Pacific Ocean circulation and climate. *Journal of Oceanology and Limnology*, *38*(4), 906–929. https://doi.org/10.1007/s00343-020-0240-1

Jackson, L., Hallberg, R., & Legg, S. (2008). A parameterization of shear-driven turbulence for ocean climate models. *Journal of Physical Oceanography*, *38*(5), 1033–1053. https://doi.org/10.1175/2007JPO3779.1

Jones, J. H. (1973). Vertical mixing in the equatorial undercurrent. *Journal of Physical Oceanography*, *3*(3), 286–296. https://doi.org/10.1175/1520-0485(1973)003<0286:VMITEU>2.0.CO;2

Kantha, L. H., & Clayson, C. A. (1994). An improved mixed layer model for geophysical applications. *Journal of Geophysical Research*, *99*(C12), 25235–25266. https://doi.org/10.1029/94JC02257

Kashino, Y., España, N., Syamsudin, F., Richards, K. J., Jensen, T., Dutrieux, P., & Ishida, A. (2009). Observations of the North Equatorial current, Mindanao current, and Kuroshio current system during the 2006/07 El Niño and 2007/08 La Niña. *Journal of Oceanography*, *65*(3), 325–333. https://doi.org/10.1007/s10872-009-0030-z

Köhler, J., Mertens, C., Walter, M., Stöber, U., Rhein, M., & Kanzow, T. (2014). Variability in the internal wave field induced by the Atlantic deep western boundary current at 16°N. *Journal of Physical Oceanography*, *44*(2), 492–516. https://doi.org/10.1175/JPO-D-13-010.1

Large, W. G., McWilliams, J. C., & Doney, S. C. (1994). Oceanic vertical mixing: A review and a model with a nonlocal boundary layer parameterization. *Review of Geophysics*, *32*(4), 363–403. https://doi.org/10.1029/94RG01872

Li, J., & Gan, J. (2020). On the formation dynamics of the North equatorial undercurrent. *Journal of Physical Oceanography*, *50*(5), 1399–1415. https://doi.org/10.1175/JPO-D-19-0142.1

Li, J., & Gan, J. (2022a). Characteristics and formation of the Luzon Undercurrent in the western North Pacific: Observational study. *Journal of Geophysical Research: Oceans*, *127*(7), e2022JC018968. https://doi.org/10.1029/2022JC018968

Li, J., & Gan, J. (2022b). On the north equatorial current spatiotemporal modes and responses in the western boundary currents. *Progress in Oceanography*, *205*, 102820. https://doi.org/10.1016/j.pocean.2022.102820

Lien, R.-C., Ma, B., Lee, C. M., Sanford, T. B., Mensah, V., Centurioni, L. R., et al. (2015). The Kuroshio and Luzon undercurrent east of Luzon Island. *Oceanography*, *28*(4), 54–63. https://doi.org/10.5670/oceanog.2015.81

Lin, H., Liu, Z., Hu, J., Menemenlis, D., & Huang, Y. (2020). Characterizing meso-to submesoscale features in the South China Sea. *Progress in Oceanography*, *188*, 102420. https://doi.org/10.1016/j.pocean.2020.102420

Liu, Z., & Gan, J. (2016). Open boundary conditions for tidally and subtidally forced circulation in a limited-area coastal model using the Regional Ocean Modeling System (ROMS). *Journal of Geophysical Research: Oceans*, *121*(8), 6184–6203. https://doi.org/10.1002/2016JC011975

Masumoto, Y., Sasaki, H., Kagimoto, T., Komori, N., Ishida, A., Sasai, Y., et al. (2004). A fifty-year eddy-resolving simulation of the world ocean: Preliminary outcomes of OFES (OGCM for the Earth Simulator). *Journal of Earth Simulator*, *1*, 35–56.

McWilliams, J. C. (2016). Submesoscale currents in the ocean. *Proceedings of the Royal Society A: Mathematical, Physical and Engineering Sciences*, *472*(2189), 20160117. https://doi.org/10.1098/rspa.2016.0117

Mellor, G. L., & Blumberg, A. F. (1985). Modeling vertical and horizontal diffusivities with the sigma coordinate system. *Monthly Weather Review*, *113*(8), 1379–1383. https://doi.org/10.1175/1520-0493(1985)113<1379:MVAHDW>2.0.CO;2

Mellor, G. L., & Yamada, T. (1974). A hierarchy of turbulence closure models for planetary boundary layers. *Journal of the Atmospheric Sciences*, *31*(7), 1791–1806. https://doi.org/10.1175/1520-0469(1974)031<1791:AHOTCM>2.0.CO;2

Mellor, G. L., & Yamada, T. (1982). Development of a turbulence closure model for geophysical fluid problems. *Review of Geophysics*, *20*(4), 851–875. https://doi.org/10.1029/RG020i004p00851

Molemaker, M. J., McWilliams, J. C., & Yavneh, I. (2005). Baroclinic instability and loss of balance. *Journal of Physical Oceanography*, *35*(9), 1505–1517. https://doi.org/10.1175/JPO2770.1

Monin, A. S., & Yaglom, A. M. (1971). *Statistical fluid mechanics: The mechanics of turbulence*. In (p. 769). MIT Press.

Munk, W. H., & Anderson, E. R. (1948). Notes on a theory of the thermocline. *Journal of Marine Research*, *7*(3), 276–295.

Nan, F., Xue, H., & Yu, F. (2015). Kuroshio intrusion into the South China sea: A review. *Progress in Oceanography*, *137*, 314–333. https://doi.org/10.1016/j.pocean.2014.05.012

Nitani, H. (1972). Beginning of the Kuroshio. In *Kuroshio: Its physical aspects* (pp. 129–163).

Pacanowski, R. C., & Philander, S. G. H. (1981). Parameterization of vertical mixing in numerical models of tropical oceans. *Journal of Physical Oceanography*, *11*(11), 1443–1451. https://doi.org/10.1175/1520-0485(1981)011<1443:POVMIN>2.0.CO;2

Peters, H., Gregg, M. C., & Toole, J. M. (1988). On the parameterization of equatorial turbulence. *Journal of Geophysical Research*, *93*(C2), 1199–1218. https://doi.org/10.1029/JC093iC02p01199

Qiu, B., & Lukas, R. (1996). Seasonal and interannual variability of the North Equatorial current, the Mindanao current, and the Kuroshio along the Pacific western boundary. *Journal of Geophysical Research*, *101*(C5), 12315–12330. https://doi.org/10.1029/95JC03204

Qiu, B., Rudnick, D. L., Chen, S., & Kashino, Y. (2013). Quasi-stationary North equatorial undercurrent jets across the tropical North Pacific Ocean. *Geophysical Research Letters*, *40*(10), 2183–2187. https://doi.org/10.1002/grl.50394

Qu, T., Chiang, T.-L., Wu, C.-R., Dutrieux, P., & Hu, D. (2012). Mindanao Current/Undercurrent in an eddy-resolving GCM. *Journal of Geophysical Research*, *117*(C6), C06026. https://doi.org/10.1029/2011JC007838

Qu, T., Kagimoto, T., & Yamagata, T. (1997). A subsurface countercurrent along the east coast of Luzon. *Deep-Sea Research, Part A: Oceanographic Research Papers I*, *44*(3), 413–423. https://doi.org/10.1016/S0967-0637(96)00121-5

Samelson, R. M. (1998). Large-scale circulation with locally enhanced vertical mixing. *Journal of Physical Oceanography*, *28*(4), 712–726. https://doi.org/10.1175/1520-0485(1998)028<0712:LSCWLE>2.0.CO;2

Sasaki, H., Nonaka, M., Masumoto, Y., Sasai, Y., Uehara, H., & Sakuma, H. (2008). An eddy-resolving hindcast simulation of the quasiglobal ocean from 1950 to 2003 on the Earth Simulator. In *High resolution numerical modelling of the atmosphere and ocean* (pp. 157–185). Springer New York. https://doi.org/10.1007/978-0-387-49791-4_10

Schönau, M. C., & Rudnick, D. L. (2017). Mindanao Current and Undercurrent: Thermohaline structure and transport from repeat glider observations. *Journal of Physical Oceanography*, *47*(8), 2055–2075. https://doi.org/10.1175/JPO-D-16-0274.1

Shchepetkin, A. F., & McWilliams, J. C. (2005). The regional oceanic modeling system (ROMS): A split-explicit, free-surface, topography-following-coordinate oceanic model. *Ocean Modelling*, *9*(4), 347–404. https://doi.org/10.1016/j.ocemod.2004.08.002

Song, Y., & Haidvogel, D. (1994). A semi-implicit ocean circulation model using a generalized topography-following coordinate system. *Journal of Computational Physics*, *115*(1), 228–244. https://doi.org/10.1006/jcph.1994.1189

Stone, P. H. (1970). On non-geostrophic baroclinic stability: Part II. *Journal of the Atmospheric Sciences*, *27*(5), 721–726. https://doi.org/10.1175/1520-0469(1970)027<0721:ONGBSP>2.0.CO;2

Storer, B. A., Buzzicotti, M., Khatri, H., Griffes, S. M., & Aluie, H. (2022). Global energy spectrum of the general oceanic circulation. *Nature Communications*, *13*(1), 5314. https://doi.org/10.1038/s41467-022-33031-3

Thorpe, S. A. (2007). *An introduction to ocean turbulence*. Cambridge University Press.

Wang, F., Zang, N., Li, Y., & Hu, D. (2015). On the subsurface countercurrents in the Philippine sea. *Journal of Geophysical Research: Oceans*, *120*(1), 131–144. https://doi.org/10.1002/2013JC009690

Wang, Q., Zhai, F., & Hu, D. (2014). Variations of Luzon Undercurrent from observations and numerical model simulations. *Journal of Geophysical Research: Oceans*, *119*(6), 3792–3805. https://doi.org/10.1002/2013JC009694

Yu, Z., & Schopf, P. S. (1997). Vertical eddy mixing in the tropical upper ocean: Its influence on zonal currents. *Journal of Physical Oceanography*, *27*(7), 1447–1458. https://doi.org/10.1175/1520-0485(1997)027<1447:VEMITT>2.0.CO;2

Zhang, J., Zhang, Z., & Qiu, B. (2023a). Parameterizing submesoscale vertical buoyancy flux by simultaneously considering baroclinic instability and strain-induced frontogenesis. *Geophysical Research Letters*, *50*(8), e2022GL102292. https://doi.org/10.1029/2022GL102292

Zhang, Z. (2024). Submesoscale dynamic processes in the South China sea. *Ocean-Land-Atmosphere Research*, *3*, 0045. https://doi.org/10.34133/olar.0045

Zhang, Z., Liu, Y., Qiu, B., Luo, Y., Cai, W., Yuan, Q., et al. (2023b). Submesoscale inverse energy cascade enhances southern ocean eddy heat transport. *Nature Communications*, *14*(1), 1335. https://doi.org/10.1038/s41467-023-36991-2